

1 **The amino acid sequence determines protein abundance through**
2 **its conformational stability and reduced synthesis cost.**

3
4 Filip Buric^{1*}, Sandra Viknander^{1*}, Xiaozhi Fu¹, Oliver Lemke², Jan Zrimec^{1,3}, Lukasz Szyrwiak²,
5 Michael Mueleder⁴, Markus Ralser², Aleksej Zelezniak^{1,5,6†}

6
7 1 - Department of Biology and Biological Engineering, Chalmers University of Technology,
8 Kemivägen 10, SE-412 96, Gothenburg, Sweden

9 2 - Department of Biochemistry, Charité – Universitätsmedizin Berlin, 10117 Berlin, Germany

10 3 - Department of Biotechnology and Systems Biology, National Institute of Biology, Večna pot
11 111, SI1000 Ljubljana, Slovenia

12 4 - Core Facility High Throughput Mass Spectrometry, Charité – Universitätsmedizin Berlin, 10117
13 Berlin, Germany

14 5 - Institute of Biotechnology, Life Sciences Centre, Vilnius University, Sauletekio al. 7, LT10257
15 Vilnius, Lithuania

16 6 - Randall Centre for Cell & Molecular Biophysics, King's College London, New Hunt's House,
17 Guy's Campus, SE1 1UL London, UK

18 *These authors contributed equally

19 †corresponding author (email: aleksej.zelezniak@chalmers.se)

20 **Keywords:** proteome, protein sequence, protein expression, protein stability, deep learning,
21 language models, explainable machine learning, molecular dynamics

22 Abstract

23 Understanding what drives protein abundance is essential to biology, medicine, and biotechnology.
24 Driven by evolutionary selection, the amino acid sequence is tailored to meet the required
25 abundance of proteomes, underscoring the intricate relationship between sequence and functional
26 demand. Yet, the specific role of amino acid sequences in determining proteome abundance remains
27 elusive. Here, we demonstrate that the amino acid sequence predicts abundance by shaping a
28 protein's conformational stability. We show that increasing the abundance provides metabolic cost
29 benefits, underscoring the evolutionary advantage of maintaining a highly abundant and stable
30 proteome. Specifically, using a deep learning model (BERT), we predict 56% of protein abundance
31 variation in *Saccharomyces cerevisiae* solely based on amino acid sequence. The model reveals
32 latent factors linking sequence features to protein stability. To probe these relationships, we
33 introduce MGEM (Mutation Guided by an Embedded Manifold), a methodology for guiding protein
34 abundance through sequence modifications. We find that mutations increasing abundance
35 significantly alter protein polarity and hydrophobicity, underscoring a connection between protein
36 stability and abundance. Through molecular dynamics simulations and *in vivo* experiments in yeast,
37 we confirm that abundance-enhancing mutations result in longer-lasting and more stable protein
38 expression. Importantly, these sequence changes also reduce metabolic costs of protein synthesis,
39 elucidating the evolutionary advantage of cost-effective, high-abundance, stable proteomes. Our
40 findings support the role of amino acid sequence as a pivotal determinant of protein abundance and
41 stability, revealing an evolutionary optimization for metabolic efficiency.

42 Introduction

43 The intricate interplay between protein synthesis and degradation defines intracellular protein levels,
44 with implications for therapeutic strategies, as well as efficient protein and cellular engineering. The
45 complex regulation of protein homeostasis suggests that multiple factors contribute to the overall
46 proteome makeup, with the evolutionarily encoded sequence potentially playing a pivotal role in
47 proteome composition. For instance, protein synthesis is strongly regulated at the initiation step ^{1,2},
48 whose rate varies broadly between mRNAs, depending not only on the transcript sequence features
49 but also on the amino acids at the N-terminal ^{3,4}. In bacteria, the amino acid composition of the C-
50 terminal is a strong determinant of protein degradation rates, explaining a wide range of protein
51 abundances ^{5,6}. These, along with the multiple mechanisms of post-translational regulation ^{7,8},
52 suggest that this rather tight regulation occurs at the degradation level and is encoded, at least
53 partially, in the amino acid sequence. Empirically, amino acid composition and sequence features
54 were seen to correlate with protein abundance ⁹⁻¹¹, transcending mere codon composition influences
55 on protein abundance¹². While the importance of protein sequence in determining abundance is
56 recognised, the quantitative relationship between sequence and abundance remains elusive, as
57 does the link between the evolutionary mechanisms that underlie this relationship.

58
59 On a broader scale, proteins situated as central players in cellular processes or as critical nodes in
60 interaction networks often exhibit higher abundances ¹³. Evolutionarily, these highly abundant
61 proteins face stringent constraints, evolving at a slower pace due to their potential large-scale impact
62 on cellular fitness ^{14,15}. Remarkably, the conservation of steady-state protein abundances spans
63 across diverse evolutionary lineages, ranging from bacteria to human ¹⁶⁻¹⁸. Theoretical models
64 suggest that increasing protein abundance slows evolution due to reduced fitness, with the least
65 stable proteins adapting the fastest ¹⁹. Yet, under strong selection, proteins can evolve faster by
66 adopting mutations that enhance stability and folding ²⁰. Experimental evidence also suggests that
67 a protein's capacity to evolve is enhanced by the mutational robustness conferred by extra stability
68 ²¹⁻²³, meaning that protein stability increases evolvability by allowing a protein to accept a broader
69 range of beneficial mutations while still folding to its native structure. Thermostability gains of highly
70 expressed orthologs are often accompanied by a more negative ΔG of folding, indicating that highly
71 expressed proteins are often more thermostable ²⁴, as often explained by the so-called misfolding
72 avoidance hypothesis (MAH), because stable proteins are evolutionarily designed to tolerate
73 translational errors ²⁵⁻²⁷. On the contrary, several empirical studies revealed no substantial
74 correlation between protein stability and protein abundance ^{28,29}. Likewise, the overall cost (per
75 protein) of translation-induced misfolding is low compared to the metabolic cost of synthesis ^{30,31},
76 suggesting that MAH does not explain why highly abundant proteins evolve slower ²⁹. On the other
77 hand, cells may have fine-tuned protein sequences to balance their functional importance with the
78 metabolic costs they incur, reflecting an optimisation between functional necessity and energy

79 efficiency^{32–34}. Given the intricate interplay of evolutionary constraints, protein stability, abundance,
80 and metabolic cost, it still remains unclear how cells evolved their sequences to strike an optimal
81 balance between functional demands of proteome and cellular fitness associated with synthesis and
82 maintenance of protein abundance.

83

84 In this study, we explored the relationship between a protein's amino acid sequence and its
85 abundance. Using a deep neural network transformer (BERT) trained on data from 21 proteome
86 studies, we could predict over half of the protein copy number variation ($R^2_{\text{test}} = 56\%$) in
87 *Saccharomyces cerevisiae* based solely on amino acid sequences. Delving into the neural network's
88 self-attention mechanism to understand which protein sequence features are predictive of their
89 abundances, we revealed that the network indirectly identified specific physicochemical properties
90 inherently encoded in amino acid sequences related to a protein's conformational stability. We then
91 introduced MGEM (Mutation Guided by an Embedded Manifold) to probe sequence space and found
92 that abundance-enhancing mutations notably affected protein polarity and hydrophobicity, hinting at
93 a stability-abundance connection. Molecular dynamics simulations further confirmed the enhanced
94 stability of abundance-increasing mutants. Using a proteomics experiment in yeast, we revealed that
95 mutant protein remained more abundant over the course of yeast growth phases compared to a wild
96 type variant. Importantly, we found that mutants with increased abundance had lower amino acid
97 synthesis costs than their native versions, underscoring the fitness benefits of abundant, stable
98 proteins. Our research shows that the amino acid sequence is a key factor influencing intracellular
99 protein levels. This is achieved by boosting protein stability, which is driven by cost-effective amino
100 acid substitutions, providing evolutionary benefits by reducing the metabolic costs of protein
101 synthesis.

102

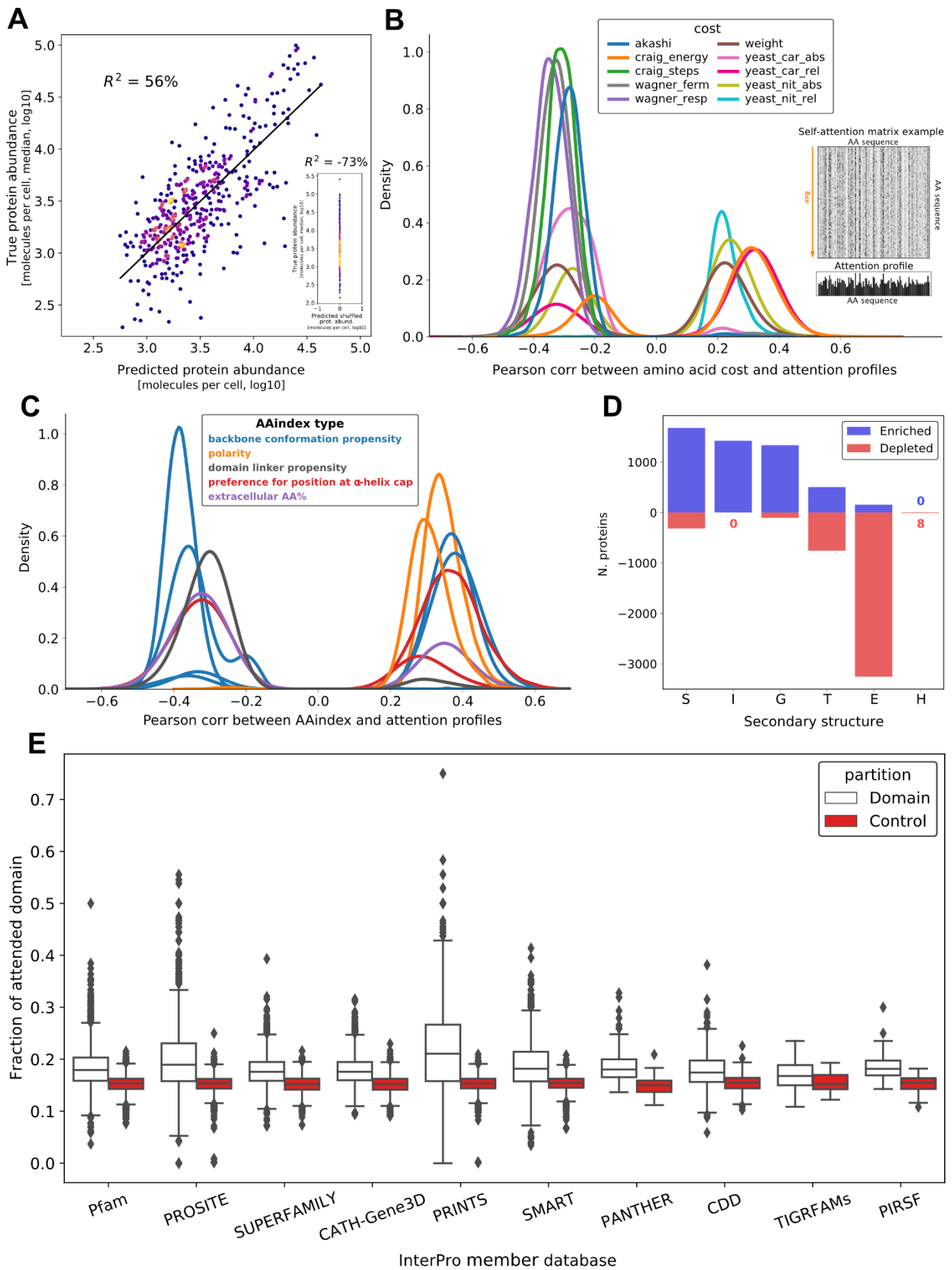
103

104 Results

105 The amino acid sequence is predictive of protein abundance.

106 To investigate the relationship between amino acid sequence and protein abundance, we used a
107 compendium of 21 experimental systematic quantitative studies employing mass spectrometry and
108 microscopy to estimate absolute protein abundances of over 5000 proteins (copy numbers per cell)
109 in *Saccharomyces cerevisiae* grown predominantly in the exponential phases across multiple
110 conditions essentially capturing proteome variation³⁵. The gene-wise dynamic range of protein
111 abundances spanned an average of 5 orders of magnitude, while individual protein expression
112 values for 95% of proteins varied within only one relative standard deviation (RSD) across all
113 experimental conditions (Figure S1). A similar phenomenon has been observed previously with
114 mRNA levels encoded in the DNA sequences^{36,37}. This result suggests that individual protein
115 expression across experimental conditions primarily fluctuates around a specific expression value,
116 suggesting its deterministic nature.

117
118 Next, to investigate the relationship between amino acids and intracellular protein levels, we
119 formulated a regression problem by utilising protein sequences to model protein abundance values.
120 To learn sequences, we chose the Bidirectional Encoder Representations from Transformers
121 (BERT) architecture^{38,39}, which allows for transparency in weighing the contributions of amino acid
122 residues on protein levels and provides insights into the most relevant sequence features the model
123 uses³⁹⁻⁴¹ to make predictions about protein abundances, using an intrinsic attention mechanism⁴².
124 Due to deep learning's need for extensive training data and the yeast dataset's limited size, we used
125 repeated measurements (up to 21 sequence copies from all experiments in the dataset) to account
126 for inter-experimental variability (equivalent to regression with replicates). Our augmented dataset
127 included 199,206 training examples, with 10% of random sequences uniquely chosen for validation
128 during model training and 10% for a hold-out test during final model evaluation (Methods M1). By
129 training BERT from scratch, we found that the model predicts 56% of protein abundance variation
130 ($R^2 = 56\%$ on a holdout test set) using only an amino acid sequence as input, suggesting that the
131 sequence predominantly encodes protein abundance. In contrast, the model predictions failed
132 completely when performing a randomization test with shuffled sequences ($R^2 = -73\%$, Figure 1A
133 inset), confirming that the model relies on residue interdependencies in a sequence rather than
134 simply learning amino acid frequencies when predicting protein levels. Further analysis confirmed
135 that amino acid frequency is uniformly distributed across the entire dynamic range of protein
136 abundances, with a mean CV of 7% over abundance deciles (Figure S1D), supporting the neural
137 network's ability to pick up information encoded in the sequence.



138

139 **Figure 1. The amino acid sequence is predictive of protein abundance.**

140 **A)** BERT performance on a hold-out test set, coloured by density. **Inset:** Random prediction control using
141 shuffled versions of the test sequences. The poor performance on randomized input, effectively predicting a
142 single value, demonstrates that the model has learned sequence structure and not amino acid frequencies.

143 **B)** Attention profiles correlate with amino acid metabolic costs (see also Table S1 for full description). Shown
144 are distributions across all sequences of maximum (absolute) Pearson correlations of any attention profile with
145 p-value < 1e-5. **Inset:** A BERT attention matrix example (top) and derived attention profile (bottom) for a short
146 sequence. Attention matrices consist of directional association weights between pairs of residues, normalized
147 as a percentage. The profiles were obtained by averaging along the “attends-to” axis, as the “attended-by”
148 variation is generally more informative, resulting in one-dimensional attention profiles.

149 **C)** Attention profiles correlate with 10 non-redundant AAindex variables (colored by index type), showing that
150 profiles capture information pertaining to backbone conformation, physicochemical properties, domain linkage,
151 and secondary structure. While some AAindex types correlate with attention profiles both positively and
152 negatively (e.g. backbone conformation), individual AAindex variables within these types are overall either
153 positively or negatively correlated. The categories shown span AAindex variables that are both positively and
154 negatively correlated with attention.

155 **D)** Proteins are split into two subpopulations of sequences with high attention values (z-score > 1) that are
156 either enriched in turns and helices (S, I, G, and T in DSSP notation) and, to a lesser extent, extended strand
157 (E), or largely depleted in extended strand (E) and turn (T), as assessed with one-sided hypergeometric tests
158 (p-value < 0.05).

159 **E)** Overlap of attention patterns with protein domains from the yeast InterPro database, grouped by member
160 databases. The attention coverage of domains (fraction overlapping with attention profiles) is significantly
161 higher than control for 10 out of 12 member databases (Wilcoxon two-sided signed-rank test, p-value < 0.05),
162 with the highest coverage in PRINTS and PROSITE.

163

164 The attention mechanism identifies sequence and structural features 165 linked to protein abundance.

166 Next, we wanted to interpret the features learned by the transformer which explain protein
167 abundance. Models generated by deep neural networks are often difficult to interpret⁴³, however the
168 self-attention mechanism used by transformers has been shown to match multiple physicochemical
169 properties and substitution likelihoods of amino acids⁴⁰. To increase interpretability of the model as
170 a map of sequence-to-protein abundances, we trained the model from scratch, as opposed to fine-
171 tuning pretrained large protein language models^{44–47}. Protein language embeddings, including
172 sequence representations learned from structural models⁴⁸, have been shown to have limited
173 generalization to all protein functions and properties^{49,50}, thus making it difficult to use for generalized
174 interpretation. Instead, by training the model from scratch in a regression setting, we ensured that
175 our model learned relevant sequence representations related to protein abundance, easing
176 interpretation. Thus, we next attempted to identify abundance-related links to physicochemical
177 protein features using the attention values derived from yeast protein sequences. We extracted the
178 attention weights of each input sequence and obtained one-dimensional per-residue attention
179 profiles, which reflected the average percentage of attention that each residue receives from all
180 others in the sequence when making the corresponding abundance prediction (see Figure S2 and
181 Methods M2).

182
183 To examine the determinants of protein abundance, we first correlated attention profiles with amino
184 acid costs⁵¹ (Methods M3), as amino acid synthesis cost is known to be a determinant of protein
185 abundance^{32,52–54}. The strongest correlations were found between attention profiles and the
186 energetic cost of amino acids (*craig_energy*)⁵⁵ averaged over all proteins (mean Pearson's $r = 0.32$,
187 BH adj. p -value $< 1e-5$). Conversely, anticorrelations were observed with synthetic cost under both
188 respiratory and fermentative growth (*wagner_resp*, *wagner_ferm*, respectively)⁵⁴ as well as the
189 number of synthesis steps (*craig_steps*)⁵⁵ (mean Pearson's $r = -0.35$, -0.33 , and -0.31 , respectively,
190 BH adj. p -value $< 1e-5$). Additionally, some of the systemic costs introduced by Barton et al.⁵¹ using
191 genome-scale flux balance analysis calculations⁵⁶ showed positive and negative correlations with
192 attention, such as the impact of the relative change of the amino acid requirement on the minimal
193 intake of glucose (*yeast_car_rel*, mean Pearson's $r = 0.32$ over 1855 proteins and -0.33 over 705
194 proteins) and the absolute change of the amino acid requirement on the minimal intake of ammonium
195 (*yeast_nit_abs*, mean Pearson's $r = 0.25$ over 1833 proteins and -0.28 over 1165 proteins, Figure
196 1B and Table S1). A negative correlation with synthesis cost implies that the model assigns more
197 weight to "cheaply" synthesized amino acids. In contrast, a positive correlation with energy cost
198 implies paying attention to more energy-rich amino acids when predicting protein abundance. We
199 stress that the correlations reported here do not directly link cost values to the predicted abundance,

200 but rather underline the relevant latent features learned from protein sequence that the model picked
201 up intrinsically prior to mapping sequence to protein levels.

202

203 Based on our observation that amino acid frequency is uniformly distributed across the entire
204 dynamic range of protein abundances (Figure S1D), we did not expect to find specific single amino
205 acids that would determine abundances. Instead, we hypothesized that the neural network would
206 capture higher-order interactions important for structural and functional protein features. Thus, we
207 correlated attention profiles with a subset of 18 non-redundant AAindex values representing various
208 physicochemical and biochemical protein properties⁵⁷ (see Methods M4). We identified significant
209 correlations with measures of backbone *conformation propensity* (both positively and negatively
210 correlated indices, with the strongest mean correlations being 0.38 and -0.38, respectively, p-value
211 < 1e-5), *preference for position at α -helix cap* (both positively and negatively correlated indices, with
212 the strongest mean correlations per sequence being 0.37 and -0.33, respectively, p-value < 1e-5),
213 *polarity* (highest mean correlation = 0.35, p-value < 1e-5), *domain linker propensity* (mean correlation
214 = -0.31, p-value < 1e-5), and *the composition of extracellular domains seen in membrane proteins*
215 (two protein subpopulations, one with mean correlation = 0.36, the other with mean anticorrelation =
216 -0.33, p-value < 1e-5) (Figure 1C, see Tables S2 and S3 for a detailed description). Physicochemical
217 properties of amino acids, such as polarity, have been shown to affect translation speed¹¹ and
218 protein stability⁵⁸. The correlations with backbone conformation and preference for α -helix cap
219 indicators suggest a link to secondary structure, while the correlation with domain linker propensity
220 points to the model having learned to some extent the boundaries of domain separation.

221

222 We next assessed the connection between secondary structure and attention profiles by analyzing
223 the enrichment of per-residue DSSP annotations^{59,60} in high-attention positions using AlphaFold2 -
224 generated⁴⁸ structures for 4745 yeast proteins. We counted the annotations at positions with
225 attention profile z-scores > 1 and compared them to background annotation counts across all
226 proteins (using one-sided hypergeometric tests for enrichment and depletion, p-value < 0.05)
227 (Methods M5). The results showed that attention values were enriched in turns and helices (S, I, G,
228 and T in DSSP notation) but depleted in extended strands (E) for most proteins (3254 proteins)
229 (Figure 1D). For turns (T), the protein subpopulations were more evenly split, with this structure
230 enriched in 505 proteins and depleted in 754 proteins. These findings suggest that helical structures
231 may be implicated in protein abundance, while the contribution of turns and sheets towards the model
232 prediction may be more complex.

233

234 As structural properties imply function, we also investigated whether abundance-driven attention
235 specifically focuses on any functional regions of protein sequences. We examined the extent to
236 which the attention patterns cover the domains from the *S. cerevisiae* InterPro⁶¹ database. To allow
237 for comparison with controls, we focused only on domains with a length less than half of the protein

238 sequence, analyzing a total of 18,000 domains (Methods M6). For 10 out of 12 member databases,
239 domains were significantly more covered by high attention than random regions of the same length
240 (Wilcoxon two-sided signed-rank test, adj. p-value < 0.05) (Figure 1E). The results are particularly
241 striking as our BERT model was trained from scratch, not pre-trained on domains as in the study by
242 Rao et al.³⁹. We next performed a GO enrichment analysis on proteins with well-covered domains
243 (chosen as at least 30% domain length overlapping with attention patterns, well above the random
244 control), a total of 832 domains in 517 proteins (Methods M7). From the enriched terms, GO-slim
245 terms were produced for summarization (Table S4). The enriched (Hypergeometric test, adj. p-value
246 < 0.05) biological processes are diverse and, among others, include translation, protein folding,
247 modification, and metabolic processes; the molecular functions include cytoskeletal protein binding,
248 unfolded protein binding, DNA and RNA binding, transmembrane transporter activity and others.
249 This variety points at widespread domain patterns to which the model attends across different protein
250 classes rather than specific functional motifs, which hints at the role of sequence across the entire
251 proteome. On the technical side of the attention mechanism itself, it is interesting to note that
252 domains were predominantly captured by a single (and deeper) network layer (Figure S3).

253 Navigating the sequence space to control protein abundance.

254 We next hypothesized that our model could facilitate precise control over protein abundance by
255 introducing targeted changes to the protein sequence. To achieve this, we developed a Mutation
256 procedure Guided by an Embedded Manifold (MGEM), which enables us to navigate the BERT
257 model's embedded sequence manifold and perform individual amino acid substitutions that increase
258 abundance. The approach involves traversing a uni-dimensional UMAP projection of the BERT
259 encoder's high-dimensional embedded space, which assigns a scalar importance value to each
260 residue in a sequence based on its impact on protein abundance (i.e. as determined by both position
261 and amino acid that the model learned) (Figure 2A). MGEM substitutes low-importance residues in
262 a starting wild type sequence with high-importance residues from a set of guide sequences selected
263 based on their topmost abundance levels (Figure 2B, see details in Methods M8 and M9). Thus, by
264 borrowing important amino acids (as measured by their order in the UMAP projection) from highly
265 abundant proteins, the modified sequence is “moved” towards higher abundance. This is based on
266 the posited property of the high-dimensional BERT embedded space by which the sequence
267 representations are approximately ordered (or “ranked”) according to the target value (Figure 2A).
268 The per-residue importance values obtained with UMAP are a good approximation of this ordering
269 (Spearman's $\rho = 0.8$, p-value < $1e-16$) (Figure 2C), enabling the sorting of all residues on a univariate
270 scale that spans all sequences, according to their importance towards prediction (see Methods M8).
271 Our novel method relies on the learned relationship between sequences and only minimally changes
272 wild types by deterministically substituting the individual amino acids directly related to the
273 abundance, without relying on probabilistic or stochastic optimization searches.

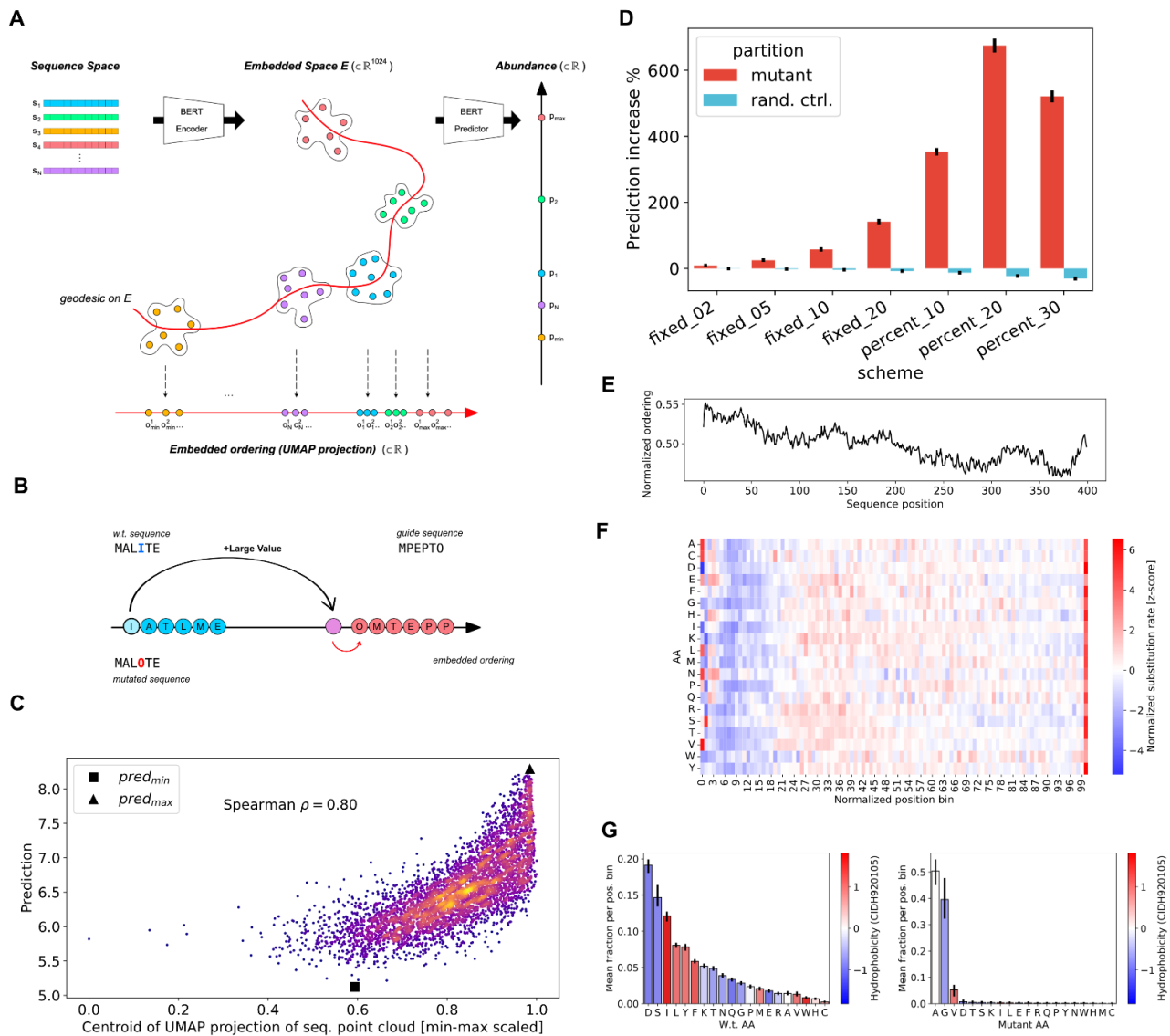
274

275 We next performed a series of *in silico* sequence perturbation experiments by introducing
276 substitutions that would increase protein abundance. This was done across the entire set of protein
277 sequences, in different substitution schemes, each consisting of changing a given number of lowest
278 importance residues per sequence (a fixed number of 2, 5, 10, and 20 residues, as well as 10%,
279 20%, and 30% of residues in each sequence). We observed that MGEM enables control of target
280 values (protein abundance) significantly more than a random control (paired t-test, adj. p-value <1e-
281 16 for all schemes) in which a random set of residues of the same size as the MGEM set for the
282 given scheme was selected and mutated to random amino acids (Figure 2D). Indeed, on average,
283 random mutations yielded a decrease in protein abundance. The greatest MGEM increase was
284 obtained when mutating 20% of the sequence, achieving an average 675% predicted abundance
285 increase.

286

287 By inspecting MGEM mutants, we discovered that in terms of sequence position, the N-terminus is
288 the most important for abundance prediction. The average wild type embedded ordering
289 (importance) profile peaks over the leading 20% of the sequence (Figure 2E), and as a consequence
290 of the MGEM selection process, results in most amino acids being left unchanged in this region
291 (Figure 2F). Additionally, there is a much shorter hotspot of frequently mutated amino acids at the
292 very last positions of the C-terminus. In accordance with other studies^{3,4}, this would suggest that the
293 N-terminus is generally evolutionarily optimized for expression efficiency. Indeed, the composition of
294 the first 30% of sequences significantly differs from the composition of the full sequences (one-sided
295 hypergeometric test, p-value < 1e-3), with the leading region enriched in Ala (A), His (H), Met (M),
296 Pro (P), Gln (Q), Arg (R), Ser (S), Thr (T) (Table S5). The observation that distributions of substituted
297 amino acids differ from the above (some are replaced uniformly across the entire sequence length)
298 is another indication of the role of both the position and the nature of the amino acid. In terms of
299 replacement amino acids, we observed that the vast majority are A, G, and V (Figure 2G). In terms
300 of physicochemical AAindex variables, mutants show significant perturbations (paired t-test, p-value
301 < 1e-80) (see Table S6 and Figure S4), especially in indices that describe *polarity* (specifically
302 amphiphilicity, with a 19% average decrease), *backbone conformation propensity* (with the largest
303 index average decrease by 18% and the highest average index increase by 9%), and in the
304 *preference for position at α -helix cap* (average decrease by 5%), which suggests a change in the
305 likely secondary structure and a shift towards higher hydrophobicity in the mutants.

306



307

308

309

310

311

312

313

314

315

316

317

318

319

320

321

322

323

Figure 2. Navigating the sequence space to control protein abundance through guided mutation.

A) Conceptual illustration showing the posited structure of the BERT encoder embedded space and the embedded ordering construction that supports our guided mutation procedure. The encoder maps each residue in a sequence to a high-dimensional point in the embedded space E and sequences thus appear as point clouds. From a point cloud, a thin feedforward predictor yields an abundance prediction. The embedded space is posited to be structured in such a way as to allow a “traversal” of the point clouds, on a path or *geodesic* between all points (curved red line) connecting the points that are part of the lowest abundance sequences to the highest, in an increasing order of predicted values. This path in high-dimensional space is approximated with a parametric UMAP projection from the embedded space E to a single dimension, thus giving a simple linear ranking (or ordering) σ_j for each residue j , in each sequence i . This ranking serves to indicate the global weight of a given residue towards the final prediction, compared with all other residues across all sequences.

B) Simplified illustration of MGEM (mutation guided by embedded manifold) procedure, which takes advantage of the global embedded order value (“importance”) obtained for each residue, across all sequences. The residues with the lowest order value in a sequence are selected for substitution (the “I” residue at position 4 in

324 the illustration) and their order values are increased by a large amount, as a higher value would yield a greater
325 abundance. As we do not have an inverse mapping from this new value to an amino acid, we find the substitute
326 by taking “inspiration” from guide sequences, chosen as the top 10 highest abundance sequences. The residue
327 with closest ordering value to the newly increased value (“O” in the example) is taken and this amino acid
328 replaces the original one in the wild type sequence.

329 **C)** The UMAP projection is a good approximation of the embedded manifold, as it generally correlates well
330 with abundance (Spearman p-value $< 1e-308$) (the plot is colored by density). Each point corresponds to the
331 centroid of a sequence point cloud, projected through the learned UMAP function. The horizontal axis is
332 normalized to the smallest and largest values in the set of projected points. The centroid of the lowest
333 abundance sequence is marked with a black square and that of the highest abundance sequence with a black
334 triangle. The approximation is worse for lower abundance sequences, as the red square should have appeared
335 as the minimum ordering value.

336 **D)** Predicted abundance increase on sequences mutated with MGEM (black bars showing averages, with 95%
337 confidence intervals). An increasingly higher number of residues with lowest ordering (2, 5, 10, 20 residues,
338 as well as 10%, 20%, and 30% of the sequence) were selected in each scheme shown in the figure. The
339 highest overall increase occurred for the scheme consisting of mutating the 20% lowest-order residues. All
340 schemes showed significantly higher values than random control (blue), which on average decreases predicted
341 abundance.

342 **E)** The most important part of the sequence for the model is the N-terminus, as measured by the embedded
343 ordering value, here normalized to the inverse ranking of residue values (as the relative order is the important
344 information) divided by sequence length. The plot shows the average such profile for sequences of length 200
345 to 400, the profiles of which were upsampled by linear interpolation to maximum length.

346 **F)** The high importance of the N-terminus for abundance leads to fewer residues being mutated by MGEM, as
347 a consequence of the embedded ordering values (shown in F). Except for the first few positions in the
348 sequence, most amino acids in the leading 20% of the sequence are generally untouched (the leading M is
349 avoided by MGEM). The plot shows for each amino acid the normalized MGEM substitution rate over sequence
350 length bins spanning the leading 30% of sequences (computed over all sequences and mutation schemes).
351 The position has been normalized to sequence length and binned to 2 decimals (resulting in 100 bins). For
352 each amino acid, the number of times MGEM has replaced it in a bin was divided by the wild type count of that
353 amino acid in the same bin. The z-scores of these values were obtained separately for each amino acid.

354 **G)** Average fraction of wild type (left) and MGEM mutant (right) amino acid over the leading 30% of all mutated
355 sequences (error bars showing 95% confidence intervals). The amino acids are colored by their normalized
356 hydrophobicity⁶², which highlights the overall mutation shift toward more hydrophobic proteins. The binning
357 was performed as in F), i.e. over 30 of the position 100 bins for each sequence.

358 Highly abundant proteins show greater conformational stability at a 359 lower metabolic cost.

360 Mutational analysis from MGEM indicates increased protein abundance primarily from non-polar A,
361 G, V amino acid substitutions (Figure 2G). Alanine is known to stabilize helices while glycine varies
362 in its effects⁶³. Glycine can enhance stability in β -turns⁶⁴. Valine is common in thermophilic proteins
363⁵⁸, and both alanine and valine substitutions often show similar helix impacts⁶⁵. Cysteine,
364 infrequently substituted by our procedure (Figure 2G), is vital for stability due to its potential for
365 disulfide bridge formation⁶⁶. Likewise, it has been observed that highly expressed proteins are often
366 more thermostable^{24,67}. Using our method which allows for mutations that increase protein
367 abundance, we sought to determine if the model-learned sequence to abundance mapping is linked
368 to overall protein stability. To corroborate this, we applied molecular dynamics (MD) simulations to
369 100 pairs (mutant and wild types, WTs) of non-membrane yeast proteins (Figure 2D, 20% mutation
370 regime). Both mutated and their original WT versions were modeled using AlphaFold2 structures
371 (Methods M10) and molecular systems were simulated for 100 ns. While our model does account
372 for entire protein abundance variation (Figure 1A), there is a risk that introduced mutations could
373 destabilize proteins. Therefore, we only considered WT and mutant pairs that converged at the end
374 of the simulation trajectory (Methods M10) considering ~46% of the simulations in our subsequent
375 analyses. To quantify the degree of protein backbone conformational changes, we started by first
376 comparing the fluctuations of atomic positions, expressed as the standard deviation of residue alpha
377 carbons across the entire course of the MD trajectory (root mean square fluctuations, RMSF)
378 between mutant and WT sequences. 33% of converged systems showed significantly lower RMSF
379 in comparison to WT proteins (Wilcoxon rank sum test, adj. p-value < 1e-2) (Figure 3A, Figure S5).
380 Decreases in protein backbone fluctuations might be a sign of protein stabilization⁶⁸⁻⁷⁰. 59% of
381 atomic fluctuations of highly abundant mutants were at least 2 standard deviations lower than the
382 corresponding positions of the WT trajectory (Figure 3B). About 81% of mutations had no direct
383 impact on atomic fluctuations, i.e. we observed changes in fluctuations in residues as high as two
384 standard deviations away from corresponding WT positions with no mutations, suggesting that
385 changes in atomic fluctuations caused by abundance-changing mutations affect overall global
386 protein dynamics, rather than just local residues (Figure 3C).

387
388 Although large structural changes from mutations can destabilize proteins^{68,71}, backbone
389 conformational changes do not directly indicate protein stability. To delve deeper, we examined
390 intermolecular interactions, specifically the number of contacts between neighboring amino acids
391 (Methods M11). Stable proteins with robust hydrophobic cores generally have more native
392 contacts⁷². In our comparison, 84% of the high-abundance mutants exhibited significantly more
393 contacts than their wild types (Wilcoxon rank sum test, adj. p-value < 1e-4) (Figure 3D, Figure S6).
394 Proteins that easily denature expose their hydrophobic core, resulting in lost hydrophobic

395 interactions and increased solvent accessibility^{68,73,74}. Investigating the effects of A, G, V
396 substitutions on hydrophobic cores, we computed the Solvent Accessible Surface Area (SASA) for
397 all proteins. We found a significant decrease (Wilcoxon rank sum test, p-value < 1e-4) in SASA for
398 abundance-increasing mutants versus wild types, supporting our hypothesis (Figure 3E).

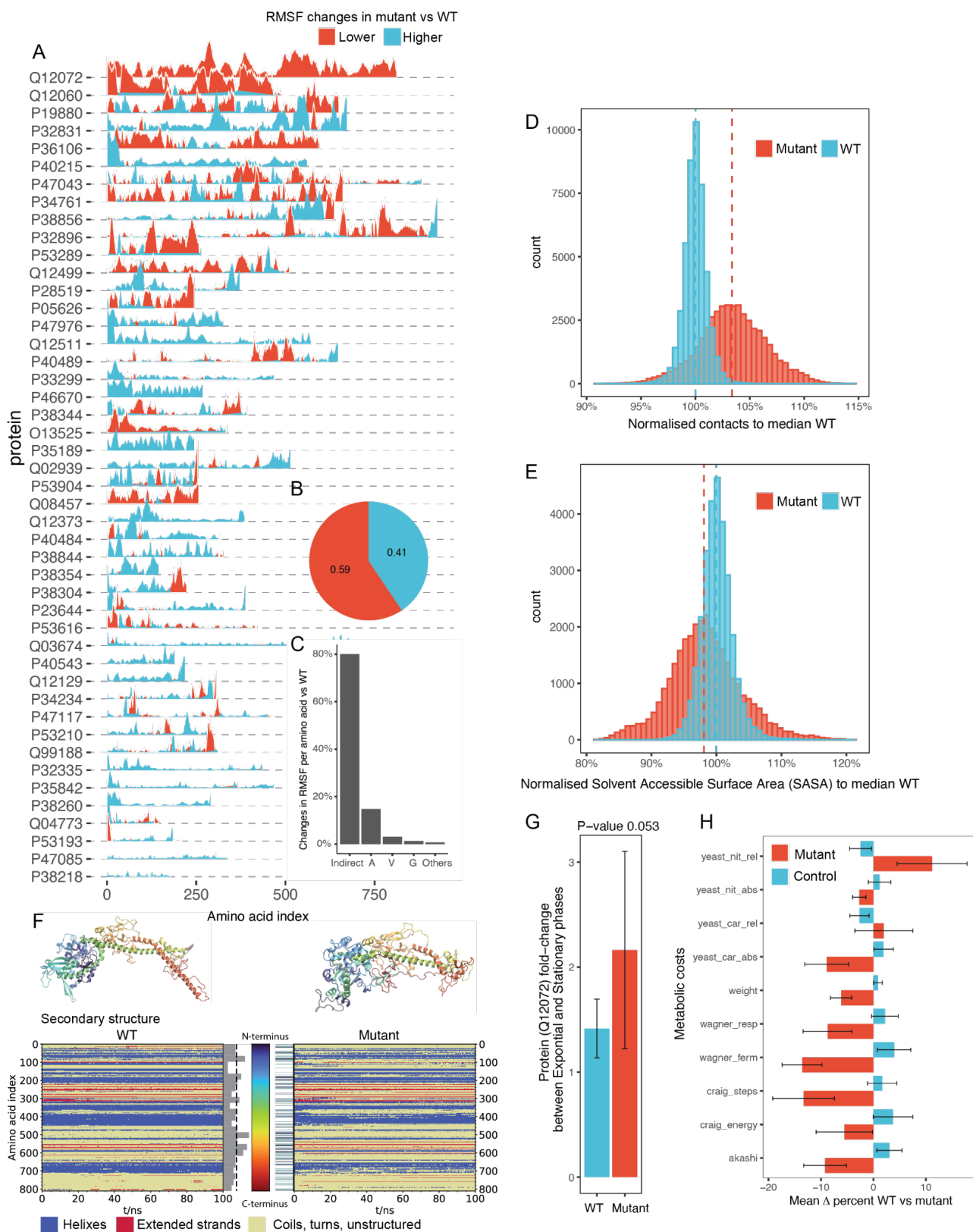
399

400 Next, we closely examined the dynamic effects of mutations on the IOC2 protein (UniprotID: Q12072)
401 based on its top decreased RMSF (Figure 3A). Although the mutant and WT IOC2 started similarly,
402 they diverged dynamically over 100 ns of simulation (Figure 3F, Figure S7). The stable core, largely
403 less mutated, differed from the more mutated C-terminal region (Figure 3F, bar plot). A notable
404 change was the breaking of an alpha-helix in the mutant, enabling the C-terminus to fold closer to
405 the protein core. This change led to an increase (WT: 53.0%, mutant: 59.9%; Mann-Whitney U test,
406 p-value < 1e-16) in the median unstructured secondary structure (Figure 3F, DSSP) but formed a
407 more compact shape than its WT counterpart. Despite imperfect alignment in the C-terminal region,
408 an overall increase in hydrophobicity is seen in the mutant (mean -0.07 with the WT vs. 0.17 with
409 the mutant, Mann-Whitney U test p-value < 1e-4), reflected in a reduced RMSF (Figure 3A, Figure
410 S5). To experimentally validate whether the abundance-increasing mutations could potentially
411 stabilize protein expression *in vivo*, we performed an experiment in *S. cerevisiae* by comparing the
412 changes in protein expression between exponential (E) and stationary (S) phases. Specifically, we
413 genetically replaced the native WT variant with the synthetically mutated IOC2 protein (Methods
414 M12). Using a liquid chromatography-coupled mass spectrometer (LC-MS) in data-independent
415 acquisition mode^{75,76}, we monitored the IOC2 expression in exponential and stationary growth
416 phases (Methods M12), growing yeast in triplicates to compare the WT and mutant variant (n = 3
417 per group). We observed that the quantified IOC2 peptides of the mutant variant were on average
418 ~50% more highly expressed (Figure 3G) between S and E phases in comparison to the WT control
419 (Methods 12), demonstrating that the mutant version of IOC2 extended the expression into the
420 stationary phase in contrast to the wild type.

421

422 Finally, we analyzed the metabolic cost implications of abundance-increasing mutants compared to
423 wild types, given concerns that increased protein copies might affect fitness¹⁹. Overall, abundance-
424 increasing mutant metabolic costs decreased significantly compared to random controls (Figure 3H,
425 paired t-test, p-value < 1e-16). The most notable reductions were in synthesis under fermentative
426 growth (*wagner_ferm*, -14% average)⁵⁴ and biosynthetic steps from central metabolism to the
427 resulting amino acid (*craig_steps*, -13% average)⁵⁵. Both factors had a strong inverse relationship
428 with BERT attention (Figure 1B & Table S1) confirming that the embedded space ordering (Figure
429 2A) and the model's attention indirectly pick up the same evolutionary phenomenon. The exceptions
430 were the impact of the relative change of the amino acid requirement on the minimal intake of
431 ammonium⁵¹ (*yeast_nit_rel*, 11% increase on average), which had the lowest correlation with
432 attention, and the impact of relative change of the amino acid requirement on the minimal intake of

433 glucose⁵¹ (*yeast_car_rel*, 2% increase on average, see Table S7 for a full list). In summary, the
434 significant cost reduction observed is especially striking since neither the BERT model nor the
435 MGEM procedure were specifically trained with cost as a factor. This suggests that the neural
436 network inherently recognized the connection between sequence cost and protein abundance,
437 aligning with earlier observations on the cost-effective metabolism of highly abundant proteomes³².
438



439

440 **Figure 3. Abundant proteins exhibit higher conformational stability and are synthesized at a**
 441 **lower cost.**

442 **A)** Root mean square fluctuations between abundance-increasing mutants and wild type (WT) structures over
 443 100 ns of molecular dynamics trajectory. **B)** Fraction of atomic fluctuation that are at least 2 standard deviations
 444 lower in mutant (red) vs wt (blue). **C)** Fraction of total significant (absolute z-score > 2) changes in RMSF per
 445 introduced mutation. Indirect denotes the regions of protein sequence with no mutations. **D)** Comparison of

446 contacts between WT and abundance-increasing mutants. Normalization is done with reference to WT using
447 frames after half of the 100 ns trajectory, contacts are considered at 8Å proximity of carbon backbone (Methods
448 M11). **E**) Comparison of solvent accessible solvent area (SASA) between WT and abundance-increasing
449 mutants. Normalization is done with reference to WT using frames after half of the 100 ns trajectory. **F**)
450 Structure (top) and DSSP plot (bottom) of the wild type (left) and the mutant (right) of IOC2 yeast protein. The
451 structures represent the last frame of the respective simulation (100 ns). The coloring denotes the amino acid
452 index as shown by the colorbar in the center (N-terminus: blue to C-terminus: red). In the DSSP plot, helical
453 structures are highlighted in blue, extended structures in red and everything else (e.g. coil, turn, unstructured)
454 in yellow. The bar plot represents the mutation rate per ~32 amino acids per bar; the dashed line represents
455 the average mutation rate per bar. On the right hand side the mutated spots are highlighted. **G**) Ratios of IOC2
456 (UniprotID: Q12072) peptides between exponential and stationary phases in WT and mutant strains. The
457 experiment was performed in biological triplicates (Methods M12). **H**) MGEM reduces protein cost. The
458 average sequence costs of mutants obtained with MGEM (20% mutated sequence) show significant overall
459 decrease compared with random control (paired t-test, p-value < 1e-308), particularly in terms of synthesis
460 costs (see also Table S7). The exceptions were two systemic costs from Barton et al.⁵¹, one having the lowest
461 correlation with attention (12% cost increase on average), and the other having both weakly positively and
462 negatively correlated subpopulations (2% cost increase on average).
463

464 Discussion

465
466 Intracellular protein levels are determined by a delicate interplay of synthesis, regulation, and
467 degradation. Despite the vast codon variability seen both within and between species at the DNA
468 level^{77,78}, the conservation of protein ortholog abundances across diverse evolutionary lineages
469 suggests an evolutionary imprint on amino acid sequences^{16–18}. While intricate cellular dynamics
470 play a role in immediate protein concentrations, it is likely that significant evolutionary information
471 resides within the primary sequence itself. Supporting this notion, the analysis of a consolidated
472 proteomics dataset from a comprehensive list of yeast studies³⁵ showed that, while individual protein
473 expressions vary, they mostly fluctuate around a specific value for 95% of proteins, but with the
474 difference between proteins spanning over five orders of magnitude (Figure S1). This led us to
475 postulate that amino acid sequences may inherently encode protein abundance. To explore this, we
476 trained a deep neural network to predict protein abundance accounting for over half of the variability
477 in abundance of the entire proteome dynamic range (Figure 1A, $R^2_{\text{test}} = 56\%$). By observing that
478 amino acid composition across deciles of the dynamic range of protein expression is rather uniform
479 (Figure S1), we confirmed that it is the amino acid arrangement in the sequence and not merely
480 amino acid composition that is coding for protein abundance (Figure 1A inset).

481
482 The contributions of the various protein features on abundance have been studied mostly in isolation
483 using linear models^{10,11,79}. However, given the dynamic nature of protein synthesis and degradation
484 processes and their interactions, nonlinear models that integrate or abstract over the multiple levels
485 are desired, especially given the loose coupling between some of these (e.g. the dynamic range of
486 protein abundance is larger than that of mRNA and the former have longer half-lives⁷⁹). Thus, to
487 decipher the biological insights gained by the neural network in predicting protein abundance, we
488 analyzed the patterns within the BERT self-attention mechanism. Notably, attention profiles showed
489 correlations with known protein abundance determinants (Figure 1B), including amino acid synthesis
490 costs, suggesting that the model recognised the cell's energetic currency concerning amino acid
491 synthesis. The attention mechanism identified multiple associations between residues throughout
492 the sequence, hinting at the neural network's ability to discern overarching structural and
493 physicochemical sequence patterns (Figure 1C). Our analysis further revealed that the network
494 prioritizes regions with distinct secondary structure elements and functional domains when predicting
495 protein abundance (Figure 1D, E). Moreover, the correlations found between attention, sequence
496 structure, and physicochemical properties like polarity and hydrophobicity underscore the potential
497 relationship between protein abundance and stability (Figure 1C).

498
499 The attention values in our model highlight crucial residue pairs for predicting protein abundance.
500 While this theoretically points to specific sequence positions which are important for abundance

501 prediction, understanding the encoder embedded space – a reflection of the sequence grammar
502 grasped by BERT – is more challenging. This high-dimensional space encapsulates intricate
503 sequence semantics and isn't straightforward to interpret, resulting in a "semantic gap" between
504 features and (human) meaning, often seen in deep learning models^{80,81}. To enhance our model's
505 explainability, we introduced the MGEM analytical framework. It simplifies the sequence space
506 exploration by first establishing a one-dimensional reference (Figure 2A, B), then guiding mutations
507 towards target sequence regions. Unlike methods that can produce unreliable predictions (predictor
508 pathologies)^{82–84} or local minima problems⁸⁵, MGEM deterministically modifies sequences based
509 on their mapped target value, offering a deterministic solution for amino acid substitutions, beneficial
510 for multiple applications. Furthermore, we believe this type of approach towards transparency and
511 explainability of deep models warrants further work. As a future improvement, the procedure could
512 be made free of guide sequences (and free of any bias towards these or inherent limitations
513 stemming from the choice of the guide set), by constructing or training an inverse embedded-space-
514 to-sequence mapping.

515

516 We applied the MGEM framework to perform a series of control-perturbation experiments to identify
517 amino acids and protein properties that are intrinsically related to abundance (Figure 2A, B). In
518 comparison to the random control that resulted in a decrease in protein abundance, MGEM-guided
519 mutations achieved an average abundance prediction increase of over six times compared to the
520 wild type sequences (Figure 2D). By inspecting MGEM mutants, we discovered that in terms of
521 sequence position, the N-terminus was the most important, with the majority of amino acids
522 remaining unchanged in this region (Figure 2E,F). This suggested that the N-terminus is generally
523 evolutionarily optimized for expression efficiency, which also supports why it is widely used for
524 protein expression optimization^{86–88}. A short hotspot at the very last position in the C-terminus was
525 frequently mutated, which is known as a signal involved in protein degradation^{5,6}. Besides the C-
526 terminus, however, most of the amino acids were substituted uniformly across the entire sequence
527 length, mainly with the hydrophobic amino acids A (alanine), G (glycine) and V (valine) (Figure 2G).
528 The introduction of hydrophobic amino acid residues into protein secondary structural components,
529 such as helices, sheets and turns, is known to affect a protein's conformational stability^{58,63,65}. We
530 therefore hypothesized that there is a link between increased abundance and protein structure, and
531 hence its stability.

532

533 We tested our hypothesis using extensive molecular dynamics (MD) simulations, an established
534 technique for studying protein dynamics at the atomic level^{68,89}. Our data, derived from 200 MD
535 simulations of random yeast proteins, showed that the majority of abundance-increasing mutations
536 had increased the number of protein contacts and reduced solvent accessibility as reflected in
537 reduced root mean square fluctuations (Figure 3A,D,E), phenotypes representative of stable proteins
538^{90–92} (Figure 3D,E, Figure S6). The *in vivo* yeast proteomics experiment showed that these mutations

539 resulted in sustained higher expression during growth phases (Figure 3G), further supporting our
540 hypothesis that mutations increasing abundance also enhance protein stability. Note that here we
541 kept codon frequencies the same as in the wild type strain, focusing solely on amino acid
542 substitutions without modifying native gene regulatory regions, e.g. promoters. This approach likely
543 leaves gene synthesis, transcription, and translation unaffected, while by observing long-term
544 expression during the stationary phase, we assessed whether *in vivo* protein levels differed from the
545 wild type due to changes in stability. While it is still unclear if the introduced mutations directly reduce
546 *in vivo* protein degradation via stabilization of its conformation or operate through other mechanisms,
547 our sequence perturbation experiments align well with previous observations that highly abundant
548 proteins are generally more stable^{19,30,67,93}. This phenomenon is often explained by the so-called
549 misfolding avoidance hypothesis and related hypotheses, which have dominated evolutionary
550 discussions for the past decade, all aimed at explaining the slower evolutionary rates observed with
551 highly abundant proteomes^{14,15}. An alternative explanation for the slow evolution of abundant
552 proteins suggests that higher benefits come with higher costs^{15,33,34}. However, our findings indicate
553 that proteins with mutations enhancing their stability are not only more abundant but also more cost-
554 effective to produce. This explains their evolutionary advantage, as a structurally stable protein
555 incurs fewer synthesis-associated costs to maintain consistent protein levels.

556
557 In conclusion, while the primary goal of our study was to investigate the relationship between a
558 protein's amino acid sequence and its abundance by examining a BERT network's self-attention
559 mechanism, our analysis revealed intricate connections between amino acid sequence, protein
560 abundance, and metabolic cost related to protein stability. Remarkably, even without explicit
561 conditioning on synthesis cost, both our BERT model and MGEM procedure succeeded in
562 uncovering these latent relationships. This demonstrates the power of deep neural networks to
563 decode complex biological systems. By manipulating the deep model's semantics of these latent
564 relationships, we unintentionally produced sequences optimized for cost. We demonstrate that
565 mutations leading to increased abundance also contribute to enhanced protein stability, which in turn
566 offers an evolutionary advantage by reducing the metabolic costs of protein synthesis. In addition,
567 the MGEM approach opens new avenues in protein engineering by providing a robust, targeted
568 method for amino acid substitution mapped to any continuous (real-valued) property. This has the
569 potential for the design of proteins that are not only functionally efficient but also metabolically cost-
570 effective, thereby offering a critical advantage in biotechnological applications. While no single theory
571 can likely fully explain the complex relationships between protein sequence, abundance, and
572 stability, our work identifies a critical link among these factors. By integrating insights from neural
573 network predictions, extensive MD simulations, and *in vivo* experiments, we present a unified
574 hypothesis that reaffirms the evolutionary advantage of stable, abundant proteins: they offer
575 functional efficacy at a reduced metabolic cost.

576 Methods

577 M1. Neural Network Training

578 *Saccharomyces cerevisiae* (strain S288C) protein sequences were obtained from the UniProt⁹⁴
579 reference proteome UP000002311 on 20th January 2020. To avoid technical challenges when
580 training neural networks, we restricted the set of proteins to those with a length between 100 and
581 1000 residues (yielding 5202 out of 6049 proteins). The intersection of this set with the proteins with
582 available abundance values from Ho et al.³⁵ resulted in 4750 unique sequences in our initial
583 sequence-abundance dataset. To assemble the final dataset we added repeated measurements for
584 each protein sequence, namely, each sequence appeared up to 21 times, each time with a different
585 experimental target value from the Ho et al. dataset³⁵, as in a regression with replicates, resulting in
586 99,603 training examples used as input/independent variable. Subsequently, for each sequence, a
587 shuffled version was introduced with an “effective null” target value, a very small fractional value of
588 $1e-5$ (the unit for absolute abundance is molecules per cell), to allow for power transformations,
589 resulting finally in 199,206 sequences. This was performed in order to expose the neural network to
590 nonsense counter-example sequences so that it may learn to distinguish and to facilitate sequence
591 interpretation, similar to training for classification problems^{95,96} (here, with real and nonsense
592 classes) or similar to using decoy sequences for distinguishing signal from noise in mass
593 spectrometry⁹⁷. The data was randomly partitioned as 80% training, 10% validation, and 10% test,
594 by splitting on unique sequences, i.e. ensuring repeated measurements of the same sequence were
595 placed in the same data partition to avoid data leakage. Protein sequences (X’s / independent
596 variable) and their corresponding target raw abundances (Y’s / dependent variable) were loaded as-
597 is to BERT as input lists. To make the abundance distribution mass-centered, the preprocessing was
598 configured to Box-Cox transform the raw abundances with $\lambda = -0.05155$ using the expectation-
599 maximization procedure as implemented in SciPy, on data based on medians of the initial dataset.

600
601 The training task’s preprocessing routine tokenized the sequences with the TAPE IUPAC³⁹ tokenizer,
602 each amino acid being assigned a unique integer value and the sequence flanked with special start
603 and stop integer tokens. The TAPE³⁹ implementation of the BERT *ProteinBertForValuePrediction*
604 class was adapted for the model training. The model was trained as a regression task to minimize
605 mean squared error (MSE). The model performance reported here was calculated by taking the
606 median abundance across experiments for the proteins in the hold-out test set (436 values), as the
607 test set obtained as above contained sequence repeats. The coefficient of determination was
608 calculated on median values of the hold-out test using the Scikit-learn function. Hyperparameters
609 search was performed using the BOHB algorithm⁹⁸ of the HyperBand scheduler⁹⁹ provided by the
610 Ray library¹⁰⁰. Details about model architecture and hyperparameters are provided in Tables S9-
611 S10. The best hypermodel thus found was then retrained. The best model consisted of 8 attention

612 layers with 4 heads each (see Tables S8). The model was trained on a multi-GPU cluster using a
613 mixture of A100 and V100 NVIDIA GPUs.

614 M2. Attention profile analysis

615 As it is generally unclear¹⁰¹ at which depth one might find lower or higher level features in such
616 architectures, we considered all non-redundant attention profiles for a given sequence when
617 measuring matches. Specifically, as BERT networks are known to have relatively high redundancy
618 (i.e. different layers and attention heads learn very similar weights), we performed pairwise Pearson
619 correlation of attention matrices from all layers and heads and kept only those that were uncorrelated
620 ($r < 0.01$) with the majority (at least 90%) of other matrices, for each sequence. This left on average
621 4 non-redundant attention matrices per sequence. Moreover, attention matrices exhibited strong
622 asymmetry (see Figure S2), often consisting of effectively uniform vertical streaks (i.e. the majority
623 of residues “attend to” a single residue near-uniformly), thus making the “attended-by” values more
624 informative (i.e. which residues receive such attention from all others). These “attended-by” values
625 were averaged to produce one-dimensional attention profiles, which could be correlated with various
626 per-residue measures. To match against qualitative data such as protein domains, we extracted
627 residue attention *patterns* by keeping only the sequence positions that had an attention value z-
628 score of at least 1 in the corresponding profile, to keep only those positions with the most signal.

629 M3. Cost analysis

630 Per-residue cost profiles were computed for all proteins in the dataset (N = 4750) using the *S.*
631 *cerevisiae* amino acid costs from Barton et al.⁵¹, with the exception of *yeast_sul_abs*, and
632 *yeast_sul_rel*, which were deemed trivial for this task since they featured zero cost for all but a few
633 amino acids. These profiles were then Pearson-correlated to all attention profiles for each protein
634 (on average 4 attention profiles per protein), keeping only the maximum correlation with p-value <
635 $1e-5$ for each protein. The p-value was set using the Bonferroni correction for multiple testing at a
636 target threshold of 0.05, thus resulting in $0.05 / 4750 = 1.053e-05$.

637 M4. AAindex Correlations

638 All 544 AAindex measures (<https://www.genome.jp/aaindex>, release 9.1 2006) were computed on a
639 subsample of 1000 *S. cerevisiae* proteins using the R package Bio3D 2.4-3¹⁰². An average absolute
640 correlation matrix was computed across the protein sequence subset and the AA indices were
641 filtered using the R *findCorrelation* function (with a cutoff of 0.5) from the *caret* package 6.0-88, to
642 only keep a non-redundant subset of 18 AA indices: BUNA790103, FINA910104, GEOR030103,
643 GEOR030104, LEVM760103, MITS020101, NADH010107, NAKH920107, PALJ810107,
644 QIAN880138, RICJ880104, RICJ880117, ROBB760107, TANS770102, TANS770108,

645 VASM830101, WERD780103, WOEC730101. These per-sequence profiles for these indices were
646 then computed for all proteins in the dataset ($N = 4750$) and Pearson-correlated to all attention
647 profiles. Only the maximum correlation with p -value $< 1e-5$ was kept for each protein. The p -value
648 was set using the Bonferroni correction for multiple testing at a target threshold of 0.05, thus resulting
649 in $0.05 / 4750 = 1.053e-05$. Note that the polar requirement (WOEC730101) was not part of the non-
650 redundant list and was added manually due to its frequent description in the literature and the low
651 correlation ($r < 0.4$) to the other indices. The resulting correlation distributions were filtered to only
652 those AA indices with an absolute mean correlation of above 0.3 across all proteins.

653 M5. Secondary structure analysis (DSSP)

654 Available *S. cerevisiae* PDB files (4745) generated by AlphaFold2 were downloaded from RCSB-
655 PDB (on 2022-03-18). For each of these, DSSP 3.0.0 annotations were obtained using the
656 BioPython 1.79¹⁰³ `dssp_dict_from_pdb_file` function. For each protein and all its attention profiles (4
657 / protein, on average), DSSP annotations at positions with attention z -scores > 1 were counted. To
658 avoid small numbers for significance testing, only structures with counts > 10 were kept. For all
659 attention profiles, one-sided hypergeometric tests with a threshold p -value of 0.05 were performed
660 both for enrichment and depletion of structure annotation counts, against the total background count
661 of annotations across all proteins. Finally, this was summarized as the number of proteins that have
662 attention profiles enriched or depleted in each type of DSSP structural annotation.

663 M6. Domain analysis

664 Each InterPro domain was overlapped with the attention patterns produced for its protein (i.e. the
665 positions of the sequence with attention z -score > 1), recording the highest overlap fraction (i.e. the
666 largest fraction of *attended-to* domain residues) among all patterns produced for the sequence
667 (output from all network layers and heads). To have a balanced control set, only domains that
668 stretched to at most 50% of their protein length were kept (18,000 domains), so that the attention
669 coverage inside the domain could be weighted against that outside of it. This was done (for each
670 domain) by taking the number of high-attention positions outside the domain and dividing it by the
671 number of times the domain could fit in the outside region (i.e. the number of windows the same
672 length as the domain). This yielded an expected count corresponding to repeatedly randomly
673 sampling subsequences the same length as the domain. The coverage fractions were taken as the
674 the number of high-attention positions (either in the domain or the expected value outside) divided
675 by the length of the domain. To assess the significance of the difference in domain coverage fraction
676 distribution between attention and control, we performed a two-sided Wilcoxon signed-rank test,
677 separately for each domain member database. The adjusted p -values were < 0.05 for 10 out of 12
678 member databases, where SFLD and HAMAP differences were not significant.

679 M7. GO term enrichment analysis

680 The GO enrichment analysis for domains that overlap with attention was performed considering the
681 proteins that have well-covered domains ($\geq 30\%$ of their positions overlapping attention patterns)
682 against the full set of proteins, with the Python library GOATOOLS 1.0.15¹⁰⁴ using the Holm-
683 Bonferroni p-value correction method and a significance threshold of 0.05. To summarize the results,
684 GOATOOLS was used to obtain yeast GO slim terms (Table S4).

685 M8. Embedded Ordering

686 To assess how individual amino acids in a sequence affect the abundance prediction, we probed the
687 embedded space that the BERT encoder maps to. We call an *embedded ordering* the parametric
688 UMAP projection¹⁰⁵ that we trained to map from this space down to a one-dimensional scale. The
689 encoder's embedded space contains 1024-dimensional point clouds (one cloud for each sequence)
690 (Figure 2A), with every amino acid being assigned a (1024-dimensional) point. And because BERT
691 uses a learned positional encoding, each residue in the sequence may be assigned a different value
692 depending on position (i.e. regardless of the type of amino acid). From this space, a relatively simple
693 feed-forward network (2 weight-normalized linear layers) is used for predicting values on the real
694 line (Box-Cox-transformed protein abundances). The fundamental assumption of our construction is
695 that (good) training induces a structure on the embedded encoder space that reflects the total order
696 of abundance values (i.e. all scalar values are comparable and arranged in a strict succession).
697 Under this assumption, we posit there exists a relatively low-dimensional manifold on which a
698 geodesic connects all points in the (full) embedded space, resulting in an arrangement from lowest-
699 prediction-value point clouds to highest-prediction-value point clouds (Figure 2A). The geodesic thus
700 gives a total order within the embedded space. To retrieve a manageable approximation of the
701 geodesic (and thus, of the order), we trained a parametric UMAP projection down to one-dimensional
702 space. The embedded ordering thus constructed assigns a scalar value to each residue in the
703 sequence, reflecting its contribution to the prediction. Moreover, these scalar values reflect a global
704 ranking across the entire sequence space, i.e. lower abundance sequences will have residues with
705 overall low order values, and the converse for higher abundance sequences. This enables easy
706 assessment of the importance of each residue and enables mutation procedures.

707

708 The training set for the parametric UMAP consisted of the embedded start token point of each
709 sequence, as information from the entire sequence is "routed" through these network nodes in the
710 attention layers, and 10% of these were kept as a hold-out test set. The training was performed over
711 multiple values of the UMAP number of neighbors hyperparameter, spanning an inclusive range from
712 1% to 25% of the number of sequences in the training set (aiming to balance local versus global
713 structure). The performance was evaluated as the Spearman correlation between the centroids of
714 the UMAP-projected point clouds and the corresponding abundance targets over test sequences.

715 M9. Mutation Guided by an Embedded Manifold (MGEM)

716 The guided mutation was performed by sorting the residues according to their embedded ordering
717 value and selecting the lowest of these for substitution, a different number for each scheme: the
718 lowest 2, 5, 10, and 20 residues in each sequence, as well as the lowest 10%, 20%, and 30% of
719 residues in each sequence. The 10 highest abundance sequences were selected as guides. This
720 gives a pool of 4480 points distributed on the higher range of ordering values, available for
721 substitution. For each residue selected to be substituted, its order value was increased by a large
722 value, set as the width of the interval containing 99% of the embedded ordering (UMAP-projected)
723 values, intuitively inducing a large shift in contribution to the prediction. To obtain a substitute residue
724 that would match this shifted value, the guide sequences were used. The residue with the closest
725 ordering value to this shifted value in each guide sequence was then chosen as a substitution
726 candidate. This substitution was repeated for 10 guide sequences, and the one resulting in the
727 highest prediction increase was finally selected. Both for the guided and the random substitution, the
728 leading M residue was avoided. Random control was performed by choosing random residues (the
729 same number as for each respective scheme) and substituting them with random amino acids.

730 M10. Molecular dynamics (MD) simulations

731 We randomly subsampled 100 proteins with an increased abundance of at least 100% (from the
732 20% mutation regime, Figure 2D), ignoring transmembrane proteins. We applied molecular
733 dynamics (MD) simulations to 100 mutated non-membrane yeast proteins showing higher
734 abundance (Figure 2D, 20% mutation regime). Structures were generated both for mutated
735 sequences and their corresponding wild types using AlphaFold2⁴⁸. The structures were generated
736 utilizing the full big fantastic database (BFD) and all five CASP 14 models⁴⁸. For each sequence,
737 the structures with the highest average pLDDT score were then selected for molecular dynamics
738 simulations. Simulations were carried out using the GROMACS simulation package 2022^{106–108}, the
739 AMBER99*-ILDN force field¹⁰⁹ and the TIP3P water model¹¹⁰. The protein was centered in a
740 dodecahedron box with 1 nm distance to the box's boundaries, solvated and neutralized by adding
741 ions. The energy of the solvated system was minimized using a steepest descent algorithm (steps =
742 50,000, emtol = 1000 kJ/mol/nm, emstep = 0.01). Afterwards, the system was equilibrated for 100
743 ps in an NVT ensemble followed by a 100 ps equilibration in an NpT ensemble. For the productive
744 run an NpT ensemble was chosen using the Parrinello-Rahman barostat (ref_p = 1 bar, tau_p = 2
745 fs, compressibility = 4.5e-5 bar⁻¹)¹¹¹. The temperature was set to 300 K using the v-rescale
746 thermostat (tau = 0.1)¹¹². For all steps periodic boundary conditions were applied in all dimensions.
747 For the simulations a leap-frog integrator¹¹³ with a time-step of 2 fs was chosen. Covalent bonds
748 involving hydrogens were constrained using the LINCS algorithm (lincs_iter = 1, lines_order = 4)¹¹⁴.
749 Short range non-bonding interactions were cut off at 1 nm. For the van-der-Waals interactions a
750 Verlet-cutoff scheme (ns_type = grid, nstlist = 10 steps, DispCorr = EnerPres), for the electrostatic

751 interactions a Particle-Mesh-Ewald summation (pme_order = 4, fourierspacing = 0.16 nm)¹¹⁵ was
752 applied. For each mutant and WT version of proteins, simulations were run for 100 ns. Protein
753 coordinates were written to file every 1 ps. Simulations were considered converged if the RMSD was
754 within a 10% error margin for 80% of the time points in the final quarter (Figure S8). Only these
755 converged simulations (entire 100 ns) were selected for RMSF profile comparisons (Figure 3A).

756 M11. Analysis of MD simulations

757 For the analysis, first, the periodic boundary conditions were fixed, and afterwards, the frames were
758 rotationally and translationally fitted onto the protein atoms of the last frame of the trajectory using a
759 least-square fit as implemented in GROMACS *gmx trjconv*. RMSF values were extracted using the
760 GROMACS simulation package. Solvent accessible surface area (SASA) was computed using the
761 implementation in GROMACS *gmx sasa*. The fraction of native contacts (Q2) were calculated from
762 the last frame of the trajectory using the Python module MDAnalysis 2.2.0^{116,117}. Contacts were
763 defined as pairs of residues with an alpha carbon distance of 8Å or less. For the calculation of the
764 DSSP⁶⁰ and the solvent accessible surface area¹¹⁸ for the analysis of the protein UniprotID:Q12072
765 python package *MDTraj* 1.9.7¹¹⁹ was used. Dynamics were analyzed using VMD 1.9.4 and
766 ChimeraX 1.4¹²⁰⁻¹²². The structural images shown in Figure 3 were made with VMD. VMD is
767 developed with NIH support by the Theoretical and Computational Biophysics group at the Beckman
768 Institute, University of Illinois at Urbana-Champaign.

769

770 M12. Proteomics analysis

771 The *S. cerevisiae* IOC2 knockout strain (*ioc2Δ::kanMX*) in the BY4741 (MATa *his3Δ1 leu2Δ0*
772 *met15Δ0 ura3Δ0*) background was requested from the Yeast Knockout (YKO) Collection¹²³ in
773 Gothenburg University and used for genomic engineering in the following procedures. Predicted
774 mutant (UniprotID: Q12072) DNA sequences flanking with 90 bp overlap to the specific genome sites
775 on both ends were ordered as gene fragments from either TWIST Bioscience
776 (www.twistbioscience.com). The mutant DNA sequence was designed such that it does not change
777 original wild type codons to minimally affect the translation. The predicted mutated amino acids were
778 substituted using most frequent corresponding codon.

779 To replace the *kanMX* gene¹²³ with the mutant gene in the genome, a gRNA plasmid targeting
780 *kanMX* was constructed based on an All-In-One plasmid pML104¹²⁴. The 20 bp gRNA sequence
781 targeting at the *kanMX* gene (GCCGCGATTAAATTCCAACA) was designed with the CRISPR tool
782 in Benchling (<https://benchling.com>). Primer sets pFA6-KanMX 488-507 FWD / pML_F and pFA6-
783 KanMX 488-507 REV / f1 ori_R (Table S11) were used to amplify pML104 into 2 fragments
784 pML104.part1 and pML104.part2 with 20 bp homologous sequences on both ends and gRNA
785 sequence integrated in the pFA6-KanMX 488-507 FWD / pFA6-KanMX 488-507 REV primers.

786 pML104.part1 and pML104.part2 were ligated into a circular plasmid named as
787 pML104.gRNA_kanMX by Gibson Assembly ¹²⁵ and was sequence-verified by Eurofins
788 (<https://www.eurofins.com/>) with M13R primer (Table S11). pML104.gRNA_kanMX and mutant gene
789 was transformed into knockout strain with PEG/LiAc method ¹²⁶ and selected on synthetic minimal
790 medium without uracil (SD-URA) plates. Colonies were verified with PCR using the primer set
791 YLR095C_F / YLR095C_R (Table S1), and the amplified fragments were sequence-verified by
792 Eurofins (<https://www.eurofins.com/>) with YLR095C_F / YLR095C_R primer set. SD medium
793 supplemented with 5-fluoroorotic acid (SD+5-FOA) ¹²⁷ was used to select colonies for loss of
794 pML104.gRNA_kanMX.

795 Recombinant colonies without plasmids and the wild type BY4741 colony were picked into YPD
796 medium. After overnight growth, 1% was inoculated into 1.5 ml YPD medium in a 48 well flower plate
797 (M2P labs) and each sample had triplicates. The 48 well flower plates were cultured in 30 °C, 1200
798 rpm for either around 10 h in a Biolector (M2P labs), until the cell growth reached mid-exponential
799 phase, or 24 h until the cell growth reached stationary phase. 1 ml cells from both phases were
800 collected and washed with MilliQ water once. After centrifugation, the supernatant was removed and
801 cell pellets were kept in -80 °C until send to perform proteomics analysis at High Throughput Mass
802 Spectrometry Core Facility, Charité (Berlin, Germany). Data independent acquisition was performed
803 using the TimsTOF PRO mass spectrometer (Bruker) was coupled to the UltiMate 3000 RSL
804 (Thermo). The peptides were separated using the Waters ACQUITY UPLC HSST3 1.8 µm column
805 at 40°C using a linear gradient ramping from 2% B to 40% B in 30 minutes (Buffer A: 0.1% FA; Buffer
806 B: ACN/0.1% FA) at a flow rate of 5 µl/min. The column was washed by an increase in 1 min to 80%
807 and kept by 6 min. In the following 0.6 min the composition of B buffer was changed to 2% and
808 column was equilibrated for 3 min. For MS calibration of ion mobility dimension, three ions of Agilent
809 ESI-Low Tuning Mix ions were selected (m/z [Th], 1/K0 [Th]: 622.0289, 0.9848; 922.0097, 1.1895;
810 1221.9906, 1.3820). The dia-PASEF windows scheme was ranging in dimension m/z from 400 to
811 1200 and in dimension 1/K 0 0.6– 1.43, with 32 x 25 Th windows with Ramp Time 100 ms. Data
812 quantification was performed using the DIA-NN 1.8 software, using library-free mode. Q12072
813 protein's expression analysis in exponential and stationary phases (Figure 3G) was carried out using
814 only the peptides that were detected in both growth phases in mutant and wild types correspondingly,
815 i.e. the protein changes are calculated as fold-changes of corresponding Q12072 measured peptides
816 in each strain. For the expression experiment three biological replicates from mutant and wild type
817 were analyzed (6 samples in total). The raw mass spectrometry data have been deposited to the
818 ProteomeXchange Consortium via the PRIDE partner repository ¹²⁸ with the dataset identifier
819 PRIDE:XXXXXXX.

820 M13. Statistical analyses

821 All statistical analyses were performed using the Python (3.9) package Scipy 1.8.1¹²⁹ and R 4.2.0.
822 For data manipulation and visualization we used pandas 1.4.0 ¹³⁰, seaborn 0.12.2 ¹³¹, scikit-learn

823 0.24.2¹³², and the R tidyverse 2.0.0¹³³ package collection. Hypothesis testing was performed using
824 the non-parametric Wilcoxon Rank Sum test, unless indicated otherwise.

825 M14. Data and Software Availability

826 Scripts, training parameters, and software versions are provided in the following repository:

827 <https://github.com/fburic/protein-mgem>

828 The models and data required to reproduce figures are stored in the following Zenodo record:

829 <https://doi.org/10.5281/zenodo.8377127>

830

831 Acknowledgements

832 The study was supported by SciLifeLab fellows program (A.Z.), Swedish Research council
833 (Vetenskapsrådet) starting grant no. 2019-05356 (A.Z.), Formas early-career research grant 2019-
834 01403 (A.Z.), WALP Wallenberg Launchpad project 2021.0198 supported by the Knut and Alice
835 Wallenberg Foundation (A.Z.). A.Z. is a Marius Jakulis Jason foundation scholar. The computations
836 and data handling were enabled by resources provided by the National Academic Infrastructure for
837 Supercomputing in Sweden (NAISS) and the Swedish National Infrastructure for Computing (SNIC)
838 at the Chalmers Center for Computational Science and Engineering (C3SE), the National
839 Supercomputer Centre in Sweden (NSC) and at the High Performance Computing Center North,
840 partially funded by the Swedish Research Council through grant agreements no. 2022-06725 and
841 no. 2018-05973. We thank Mikael Öhman and Thomas Svedberg at C3SE for their technical
842 assistance. We thank Peter Dahl in Gothenburg University for offering the YKO strain. We thank Dr.
843 Xiang Jiao in Chalmers University of Technology for providing the pML104 plasmid. We thank Dr.
844 Gyorgy Abrusan and Dr. Oriol Gracia Carmona for discussions and feedback on the manuscript.

845 References

- 846 1. Laursen, B. S., Sørensen, H. P., Mortensen, K. K. & Sperling-Petersen, H. U. Initiation of
847 protein synthesis in bacteria. *Microbiol. Mol. Biol. Rev.* **69**, 101–123 (2005).
- 848 2. Merrick, W. C. & Pavitt, G. D. Protein Synthesis Initiation in Eukaryotic Cells. *Cold Spring*
849 *Harb. Perspect. Biol.* **10**, (2018).
- 850 3. Goodman, D. B., Church, G. M. & Kosuri, S. Causes and effects of N-terminal codon bias in
851 bacterial genes. *Science* **342**, 475–479 (2013).
- 852 4. Zhao, W., Liu, S., Du, G. & Zhou, J. An efficient expression tag library based on self-
853 assembling amphipathic peptides. *Microb. Cell Fact.* **18**, 91 (2019).
- 854 5. Correa Marrero, M. & Barrio-Hernandez, I. Toward Understanding the Biochemical
855 Determinants of Protein Degradation Rates. *ACS Omega* **6**, 5091–5100 (2021).
- 856 6. Weber, M. *et al.* Impact of C-terminal amino acid composition on protein expression in
857 bacteria. *Mol. Syst. Biol.* **16**, e9208 (2020).
- 858 7. Tokmakov, A. A. *et al.* Multiple post-translational modifications affect heterologous protein
859 synthesis. *J. Biol. Chem.* **287**, 27106–27116 (2012).
- 860 8. Müller, M. M. Post-Translational Modifications of Protein Backbones: Unique Functions,
861 Mechanisms, and Challenges. *Biochemistry* **57**, 177–185 (2018).
- 862 9. van den Berg, B. A. *et al.* Exploring sequence characteristics related to high-level production
863 of secreted proteins in *Aspergillus niger*. *PLoS One* **7**, e45869 (2012).
- 864 10. Cascarina, S. M. & Ross, E. D. Proteome-scale relationships between local amino acid
865 composition and protein fates and functions. *PLoS Comput. Biol.* **14**, e1006256 (2018).
- 866 11. Riba, A. *et al.* Protein synthesis rates and ribosome occupancies reveal determinants of
867 translation elongation rates. *Proc. Natl. Acad. Sci. U. S. A.* **116**, 15023–15032 (2019).
- 868 12. Ikemura, T. Codon usage and tRNA content in unicellular and multicellular organisms. *Mol.*
869 *Biol. Evol.* **2**, 13–34 (1985).
- 870 13. Jeong, H., Mason, S. P., Barabási, A. L. & Oltvai, Z. N. Lethality and centrality in protein
871 networks. *Nature* **411**, 41–42 (2001).
- 872 14. Pál, C., Papp, B. & Lercher, M. J. An integrated view of protein evolution. *Nat. Rev. Genet.* **7**,
873 337–348 (2006).
- 874 15. Zhang, J. & Yang, J.-R. Determinants of the rate of protein sequence evolution. *Nat. Rev.*
875 *Genet.* **16**, 409–420 (2015).
- 876 16. Laurent, J. M. *et al.* Protein abundances are more conserved than mRNA abundances across
877 diverse taxa. *Proteomics* **10**, 4209–4212 (2010).
- 878 17. Tuller, T. *et al.* An evolutionarily conserved mechanism for controlling the efficiency of protein
879 translation. *Cell* **141**, 344–354 (2010).
- 880 18. Schrimpf, S. P. *et al.* Comparative functional analysis of the *Caenorhabditis elegans* and
881 *Drosophila melanogaster* proteomes. *PLoS Biol.* **7**, e48 (2009).
- 882 19. Agozzino, L. & Dill, K. A. Protein evolution speed depends on its stability and abundance and
883 on chaperone concentrations. *Proc. Natl. Acad. Sci. U. S. A.* **115**, 9092–9097 (2018).
- 884 20. Zheng, J., Guo, N. & Wagner, A. Selection enhances protein evolvability by increasing
885 mutational robustness and foldability. *Science* **370**, (2020).
- 886 21. Bloom, J. D. *et al.* Evolution favors protein mutational robustness in sufficiently large
887 populations. *BMC Biol.* **5**, 29 (2007).
- 888 22. Bloom, J. D., Labthavikul, S. T., Otey, C. R. & Arnold, F. H. Protein stability promotes
889 evolvability. *Proc. Natl. Acad. Sci. U. S. A.* **103**, 5869–5874 (2006).
- 890 23. Youssef, N., Susko, E., Roger, A. J. & Bielawski, J. P. Evolution of Amino Acid Propensities
891 under Stability-Mediated Epistasis. *Mol. Biol. Evol.* **39**, (2022).
- 892 24. Luzuriaga-Neira, A. R. *et al.* Highly Abundant Proteins Are Highly Thermostable. *Genome Biol.*

- 893 *Evol.* **15**, (2023).
- 894 25. Leuenberger, P. *et al.* Cell-wide analysis of protein thermal unfolding reveals determinants of
895 thermostability. *Science* **355**, (2017).
- 896 26. Drummond, D. A. & Wilke, C. O. Mistranslation-induced protein misfolding as a dominant
897 constraint on coding-sequence evolution. *Cell* **134**, 341–352 (2008).
- 898 27. Drummond, D. A., Bloom, J. D., Adami, C., Wilke, C. O. & Arnold, F. H. Why highly expressed
899 proteins evolve slowly. *Proc. Natl. Acad. Sci. U. S. A.* **102**, 14338–14343 (2005).
- 900 28. Plata, G. & Vitkup, D. Protein Stability and Avoidance of Toxic Misfolding Do Not Explain the
901 Sequence Constraints of Highly Expressed Proteins. *Mol. Biol. Evol.* **35**, 700–703 (2018).
- 902 29. Usmanova, D. R., Plata, G. & Vitkup, D. The Relationship between the Misfolding Avoidance
903 Hypothesis and Protein Evolutionary Rates in the Light of Empirical Evidence. *Genome Biol.*
904 *Evol.* **13**, (2021).
- 905 30. Yang, J.-R., Zhuang, S.-M. & Zhang, J. Impact of translational error-induced and error-free
906 misfolding on the rate of protein evolution. *Mol. Syst. Biol.* **6**, 421 (2010).
- 907 31. Nisthal, A., Wang, C. Y., Ary, M. L. & Mayo, S. L. Protein stability engineering insights
908 revealed by domain-wide comprehensive mutagenesis. *Proc. Natl. Acad. Sci. U. S. A.* **116**,
909 16367–16377 (2019).
- 910 32. Akashi, H. & Gojobori, T. Metabolic efficiency and amino acid composition in the proteomes of
911 *Escherichia coli* and *Bacillus subtilis*. *Proc. Natl. Acad. Sci. U. S. A.* **99**, 3695–3700 (2002).
- 912 33. Cherry, J. L. Expression level, evolutionary rate, and the cost of expression. *Genome Biol.*
913 *Evol.* **2**, 757–769 (2010).
- 914 34. Gout, J.-F., Kahn, D., Duret, L. & Paramecium Post-Genomics Consortium. The relationship
915 among gene expression, the evolution of gene dosage, and the rate of protein evolution. *PLoS*
916 *Genet.* **6**, e1000944 (2010).
- 917 35. Ho, B., Baryshnikova, A. & Brown, G. W. Unification of Protein Abundance Datasets Yields a
918 Quantitative *Saccharomyces cerevisiae* Proteome. *Cell Syst* **6**, 192–205.e3 (2018).
- 919 36. Zrimec, J. *et al.* Deep learning suggests that gene expression is encoded in all parts of a co-
920 evolving interacting gene regulatory structure. *Nat. Commun.* **11**, 1–16 (2020).
- 921 37. Agarwal, V. & Shendure, J. Predicting mRNA Abundance Directly from Genomic Sequence
922 Using Deep Convolutional Neural Networks. *Cell Rep.* **31**, 107663 (2020).
- 923 38. Devlin, J., Chang, M.-W., Lee, K. & Toutanova, K. BERT: Pre-training of Deep Bidirectional
924 Transformers for Language Understanding. *arXiv [cs.CL]* (2018).
- 925 39. Rao, R. *et al.* Evaluating Protein Transfer Learning with TAPE. *Adv. Neural Inf. Process. Syst.*
926 **32**, 9689–9701 (2019).
- 927 40. Vig, J. *et al.* BERTology Meets Biology: Interpreting Attention in Protein Language Models.
928 Preprint at <https://doi.org/10.1101/2020.06.26.174417>.
- 929 41. Rao, R., Meier, J., Sercu, T., Ovchinnikov, S. & Rives, A. Transformer protein language
930 models are unsupervised structure learners. (2020).
- 931 42. Vaswani, A. *et al.* Attention is all you need. in *Advances in neural information processing*
932 *systems* 5998–6008 (2017).
- 933 43. Savage, N. Breaking into the black box of artificial intelligence. *Nature* Preprint at
934 <https://doi.org/10.1038/d41586-022-00858-1> (2022).
- 935 44. Ferruz, N., Schmidt, S. & Höcker, B. ProtGPT2 is a deep unsupervised language model for
936 protein design. *Nat. Commun.* **13**, 4348 (2022).
- 937 45. Madani, A. *et al.* Large language models generate functional protein sequences across
938 diverse families. *Nat. Biotechnol.* (2023) doi:10.1038/s41587-022-01618-2.
- 939 46. Brandes, N., Ofer, D., Peleg, Y., Rappoport, N. & Linial, M. ProteinBERT: A universal deep-
940 learning model of protein sequence and function. *Bioinformatics* **38**, 2102–2110 (2022).
- 941 47. Rives, A. *et al.* Biological structure and function emerge from scaling unsupervised learning to
942 250 million protein sequences. Preprint at <https://doi.org/10.1101/622803>.

- 943 48. Jumper, J. *et al.* Highly accurate protein structure prediction with AlphaFold. *Nature* **596**, 583–
944 589 (2021).
- 945 49. Hu, M. *et al.* Exploring evolution-aware & -free protein language models as protein function
946 predictors. *arXiv [q-bio.QM]* (2022).
- 947 50. Johnson, S. R. *et al.* Computational Scoring and Experimental Evaluation of Enzymes
948 Generated by Neural Networks. *bioRxiv* 2023–2003 (2023).
- 949 51. Barton, M. D., Delneri, D., Oliver, S. G., Rattray, M. & Bergman, C. M. Evolutionary systems
950 biology of amino acid biosynthetic cost in yeast. *PLoS One* **5**, e11935 (2010).
- 951 52. Swire, J. Selection on synthesis cost affects interprotein amino acid usage in all three domains
952 of life. *J. Mol. Evol.* **64**, 558–571 (2007).
- 953 53. Raiford, D. W. *et al.* Do amino acid biosynthetic costs constrain protein evolution in
954 *Saccharomyces cerevisiae*? *J. Mol. Evol.* **67**, 621–630 (2008).
- 955 54. Wagner, A. Energy constraints on the evolution of gene expression. *Mol. Biol. Evol.* **22**, 1365–
956 1374 (2005).
- 957 55. Craig, C. L. & Weber, R. S. Selection costs of amino acid substitutions in ColE1 and Colla
958 gene clusters harbored by *Escherichia coli*. *Mol. Biol. Evol.* **15**, 774–776 (1998).
- 959 56. Orth, J. D., Thiele, I. & Palsson, B. Ø. What is flux balance analysis? *Nat. Biotechnol.* **28**, 245
960 (2010).
- 961 57. Kawashima, S. & Kanehisa, M. AAindex: amino acid index database. *Nucleic Acids Res.* **28**,
962 374 (2000).
- 963 58. Panja, A. S., Maiti, S. & Bandyopadhyay, B. Protein stability governed by its structural
964 plasticity is inferred by physicochemical factors and salt bridges. *Sci. Rep.* **10**, 1822 (2020).
- 965 59. Touw, W. G. *et al.* A series of PDB-related databanks for everyday needs. *Nucleic Acids*
966 *Research* vol. 43 D364–D368 Preprint at <https://doi.org/10.1093/nar/gku1028> (2015).
- 967 60. Kabsch, W. & Sander, C. Dictionary of protein secondary structure: pattern recognition of
968 hydrogen-bonded and geometrical features. *Biopolymers* **22**, 2577–2637 (1983).
- 969 61. Blum, M. *et al.* The InterPro protein families and domains database: 20 years on. *Nucleic*
970 *Acids Res.* **49**, D344–D354 (2021).
- 971 62. Cid, H., Bunster, M., Canales, M. & Gazitúa, F. Hydrophobicity and structural classes in
972 proteins. *Protein Eng.* **5**, 373–375 (1992).
- 973 63. Pace, C. N., Nick Pace, C. & Martin Scholtz, J. A Helix Propensity Scale Based on
974 Experimental Studies of Peptides and Proteins. *Biophysical Journal* vol. 75 422–427 Preprint
975 at [https://doi.org/10.1016/s0006-3495\(98\)77529-0](https://doi.org/10.1016/s0006-3495(98)77529-0) (1998).
- 976 64. Trevino, S. R., Schaefer, S., Martin Scholtz, J. & Nick Pace, C. Increasing Protein
977 Conformational Stability by Optimizing β -Turn Sequence. *Journal of Molecular Biology* vol. 373
978 211–218 Preprint at <https://doi.org/10.1016/j.jmb.2007.07.061> (2007).
- 979 65. Gregoret, L. M. & Sauer, R. T. Tolerance of a protein helix to multiple alanine and valine
980 substitutions. *Fold. Des.* **3**, 119–126 (1998).
- 981 66. Sevier, C. S. & Kaiser, C. A. Formation and transfer of disulphide bonds in living cells. *Nat.*
982 *Rev. Mol. Cell Biol.* **3**, 836–847 (2002).
- 983 67. Serohijos, A. W. R., Rimas, Z. & Shakhnovich, E. I. Protein biophysics explains why highly
984 abundant proteins evolve slowly. *Cell Rep.* **2**, 249–256 (2012).
- 985 68. Zhang, D. & Lazim, R. Application of conventional molecular dynamics simulation in evaluating
986 the stability of apomyoglobin in urea solution. *Sci. Rep.* **7**, 44651 (2017).
- 987 69. Rader, A. J. Thermostability in rubredoxin and its relationship to mechanical rigidity. *Phys.*
988 *Biol.* **7**, 16002 (2009).
- 989 70. Radestock, S. & Gohlke, H. Exploiting the Link between Protein Rigidity and Thermostability
990 for Data-Driven Protein Engineering. *Engineering in Life Sciences* vol. 8 507–522 Preprint at
991 <https://doi.org/10.1002/elsc.200800043> (2008).
- 992 71. Luo, Y. & Baldwin, R. L. How Ala \rightarrow Gly mutations in different helices affect the stability of the

- 993 apomyoglobin molten globule. *Biochemistry* **40**, 5283–5289 (2001).
- 994 72. Dill, K. A., Ozkan, S. B., Shell, M. S. & Weikl, T. R. The protein folding problem. *Annu. Rev.*
995 *Biophys.* **37**, 289–316 (2008).
- 996 73. Pace, C. N., Shirley, B. A., McNutt, M. & Gajiwala, K. Forces contributing to the conformational
997 stability of proteins. *FASEB J.* **10**, 75–83 (1996).
- 998 74. Eisenhaber, F., Lijnzaad, P., Argos, P., Sander, C. & Scharf, M. The double cubic lattice
999 method: Efficient approaches to numerical integration of surface area and volume and to dot
1000 surface contouring of molecular assemblies. *J. Comput. Chem.* **16**, 273–284 (1995).
- 1001 75. Messner, C. B. *et al.* Ultra-fast proteomics with Scanning SWATH. *Nat. Biotechnol.* (2021)
1002 doi:10.1038/s41587-021-00860-4.
- 1003 76. Vowinckel, J. *et al.* Cost-effective generation of precise label-free quantitative proteomes in
1004 high-throughput by microLC and data-independent acquisition. *Sci. Rep.* **8**, 4346 (2018).
- 1005 77. Cutter, A. D., Wasmuth, J. D. & Blaxter, M. L. The evolution of biased codon and amino acid
1006 usage in nematode genomes. *Mol. Biol. Evol.* **23**, 2303–2315 (2006).
- 1007 78. Plotkin, J. B. & Kudla, G. Synonymous but not the same: the causes and consequences of
1008 codon bias. *Nat. Rev. Genet.* **12**, 32–42 (2011).
- 1009 79. Vogel, C. & Marcotte, E. M. Insights into the regulation of protein abundance from proteomic
1010 and transcriptomic analyses. *Nat. Rev. Genet.* **13**, 227–232 (2012).
- 1011 80. Wiegrefe, S. & Pinter, Y. Attention is not not Explanation. *arXiv [cs.CL]* (2019).
- 1012 81. Duan, J. & Kuo, C.-C. J. Bridging Gap between Image Pixels and Semantics via Supervision:
1013 A Survey. *arXiv [cs.CV]* (2021).
- 1014 82. Linder, J., Bogard, N., Rosenberg, A. B. & Seelig, G. A Generative Neural Network for
1015 Maximizing Fitness and Diversity of Synthetic DNA and Protein Sequences. *Cell Syst* **11**, 49–
1016 62.e16 (2020).
- 1017 83. Szegedy, C. *et al.* Intriguing properties of neural networks. *arXiv [cs.CV]* (2013).
- 1018 84. Nguyen, A., Yosinski, J. & Clune, J. Deep Neural Networks are Easily Fooled: High
1019 Confidence Predictions for Unrecognizable Images. *arXiv [cs.CV]* (2014).
- 1020 85. Bogard, N., Linder, J., Rosenberg, A. B. & Seelig, G. A Deep Neural Network for Predicting
1021 and Engineering Alternative Polyadenylation. *Cell* **178**, 91–106.e23 (2019).
- 1022 86. Wang, C. *et al.* Model-driven design of synthetic N-terminal coding sequences for regulating
1023 gene expression in yeast and bacteria. *Biotechnol. J.* **17**, e2100655 (2022).
- 1024 87. Xu, K. *et al.* Rational Design of the N-Terminal Coding Sequence for Regulating Enzyme
1025 Expression in *Bacillus subtilis*. *ACS Synth. Biol.* **10**, 265–276 (2021).
- 1026 88. Wu, Z. *et al.* Signal Peptides Generated by Attention-Based Neural Networks. *ACS Synth.*
1027 *Biol.* **9**, 2154–2161 (2020).
- 1028 89. Pikkemaat, M. G., Linssen, A. B. M., Berendsen, H. J. C. & Janssen, D. B. Molecular
1029 dynamics simulations as a tool for improving protein stability. *Protein Eng.* **15**, 185–192
1030 (2002).
- 1031 90. Robinson-Rechavi, M. & Godzik, A. Structural genomics of *thermotoga maritima* proteins
1032 shows that contact order is a major determinant of protein thermostability. *Structure* **13**, 857–
1033 860 (2005).
- 1034 91. Razvi, A. & Scholtz, J. M. Lessons in stability from thermophilic proteins. *Protein Sci.* **15**,
1035 1569–1578 (2006).
- 1036 92. Kumar, S., Tsai, C. J. & Nussinov, R. Factors enhancing protein thermostability. *Protein Eng.*
1037 **13**, 179–191 (2000).
- 1038 93. Serohijos, A. W. R., Lee, S. Y. R. & Shakhnovich, E. I. Highly abundant proteins favor more
1039 stable 3D structures in yeast. *Biophys. J.* **104**, L1–3 (2013).
- 1040 94. UniProt Consortium. UniProt: a worldwide hub of protein knowledge. *Nucleic Acids Res.* **47**,
1041 D506–D515 (2019).
- 1042 95. Gulshad, S. & Smeulders, A. Explaining with Counter Visual Attributes and Examples. in

- 1043 *Proceedings of the 2020 International Conference on Multimedia Retrieval* 35–43 (Association
1044 for Computing Machinery, 2020).
- 1045 96. Elliott, A., Law, S. & Russell, C. Explaining classifiers using adversarial perturbations on the
1046 perceptual ball. in *2021 IEEE/CVF Conference on Computer Vision and Pattern Recognition*
1047 (CVPR) 10693–10702 (IEEE, 2021).
- 1048 97. Käll, L., Storey, J. D., MacCoss, M. J. & Noble, W. S. Assigning significance to peptides
1049 identified by tandem mass spectrometry using decoy databases. *J. Proteome Res.* **7**, 29–34
1050 (2008).
- 1051 98. Falkner, S., Klein, A. & Hutter, F. BOHB: Robust and Efficient Hyperparameter Optimization at
1052 Scale. in *Proceedings of the 35th International Conference on Machine Learning* (eds. Dy, J. &
1053 Krause, A.) vol. 80 1437–1446 (PMLR, 2018).
- 1054 99. Li, L., Jamieson, K., DeSalvo, G., Rostamizadeh, A. & Talwalkar, A. Hyperband: A novel
1055 bandit-based approach to hyperparameter optimization. *J. Mach. Learn. Res.* **18**, 6765–6816
1056 (2017).
- 1057 100. Moritz, P. *et al.* Ray: A distributed framework for emerging AI applications. in *13th*
1058 *USENIX Symposium on Operating Systems Design and Implementation (OSDI'18)* 561–
1059 577 (2018).
- 1060 101. Rogers, A., Kovaleva, O. & Rumshisky, A. A primer in bertology: What we know about how
1061 bert works. *Transactions of the Association for Computational Linguistics* **8**, 842–866 (2020).
- 1062 102. Grant, B. J., Rodrigues, A. P. C., ElSawy, K. M., McCammon, J. A. & Caves, L. S. D. Bio3d:
1063 an R package for the comparative analysis of protein structures. *Bioinformatics* **22**, 2695–2696
1064 (2006).
- 1065 103. Cock, P. J. A. *et al.* Biopython: freely available Python tools for computational molecular
1066 biology and bioinformatics. *Bioinformatics* **25**, 1422–1423 (2009).
- 1067 104. Klopfenstein, D. V. *et al.* GOATOOLS: A Python library for Gene Ontology analyses. *Sci. Rep.*
1068 **8**, 10872 (2018).
- 1069 105. Sainburg, T., McInnes, L. & Gentner, T. Q. Parametric UMAP embeddings for representation
1070 and semi-supervised learning. *arXiv [cs.LG]* (2020).
- 1071 106. Van Der Spoel, D. *et al.* GROMACS: fast, flexible, and free. *J. Comput. Chem.* **26**, 1701–1718
1072 (2005).
- 1073 107. Hess, B., Kutzner, C., van der Spoel, D. & Lindahl, E. GROMACS 4: Algorithms for Highly
1074 Efficient, Load-Balanced, and Scalable Molecular Simulation. *J. Chem. Theory Comput.* **4**,
1075 435–447 (2008).
- 1076 108. Berendsen, H. J. C., van der Spoel, D. & van Drunen, R. GROMACS: A message-passing
1077 parallel molecular dynamics implementation. *Comput. Phys. Commun.* **91**, 43–56 (1995).
- 1078 109. Aliev, A. E. *et al.* Motional timescale predictions by molecular dynamics simulations: case
1079 study using proline and hydroxyproline sidechain dynamics. *Proteins* **82**, 195–215 (2014).
- 1080 110. Jorgensen, W. L., Chandrasekhar, J., Madura, J. D., Impey, R. W. & Klein, M. L. Comparison
1081 of simple potential functions for simulating liquid water. *J. Chem. Phys.* **79**, 926–935 (1983).
- 1082 111. Parrinello, M. & Rahman, A. Polymorphic transitions in single crystals: A new molecular
1083 dynamics method. *J. Appl. Phys.* (1981).
- 1084 112. Bussi, G., Donadio, D. & Parrinello, M. Canonical sampling through velocity rescaling. *J.*
1085 *Chem. Phys.* **126**, 014101 (2007).
- 1086 113. Hockney, R. W., Goel, S. P. & Eastwood, J. W. Quiet high-resolution computer models of a
1087 plasma. *J. Comput. Phys.* **14**, 148–158 (1974).
- 1088 114. Hess, B., Bekker, H., Berendsen, H. J. C. & Fraaije, J. G. E. M. LINCS: A linear constraint
1089 solver for molecular simulations. *J. Comput. Chem.* **18**, 1463–1472 (1997).
- 1090 115. Darden, T., York, D. & Pedersen, L. Particle mesh Ewald: An N-log(N) method for Ewald sums
1091 in large systems. *J. Chem. Phys.* **98**, 10089–10092 (1993).
- 1092 116. Michaud-Agrawal, N., Denning, E. J., Woolf, T. B. & Beckstein, O. MDAAnalysis: a toolkit for the

- 1093 analysis of molecular dynamics simulations. *J. Comput. Chem.* **32**, 2319–2327 (2011).
- 1094 117. Gowers, R. *et al.* MDAnalysis: A python package for the rapid analysis of molecular dynamics
1095 simulations. in *Proceedings of the 15th Python in Science Conference (SciPy, 2016)*.
1096 doi:10.25080/majora-629e541a-00e.
- 1097 118. Shrake, A. & Rupley, J. A. Environment and exposure to solvent of protein atoms. Lysozyme
1098 and insulin. *J. Mol. Biol.* **79**, 351–371 (1973).
- 1099 119. McGibbon, R. T. *et al.* MDTraj: A Modern Open Library for the Analysis of Molecular Dynamics
1100 Trajectories. *Biophys. J.* **109**, 1528–1532 (2015).
- 1101 120. Pettersen, E. F. *et al.* UCSF ChimeraX: Structure visualization for researchers, educators, and
1102 developers. *Protein Sci.* **30**, 70–82 (2021).
- 1103 121. Goddard, T. D. *et al.* UCSF ChimeraX: Meeting modern challenges in visualization and
1104 analysis. *Protein Sci.* **27**, 14–25 (2018).
- 1105 122. Meng, E. C., Pettersen, E. F., Couch, G. S., Huang, C. C. & Ferrin, T. E. Tools for integrated
1106 sequence-structure analysis with UCSF Chimera. *BMC Bioinformatics* **7**, 339 (2006).
- 1107 123. Winzeler, E. A. Functional Characterization of the *S. cerevisiae* Genome by Gene Deletion
1108 and Parallel Analysis. *Science* vol. 285 901–906 Preprint at
1109 <https://doi.org/10.1126/science.285.5429.901> (1999).
- 1110 124. Laughery, M. F. *et al.* New vectors for simple and streamlined CRISPR-Cas9 genome editing
1111 in *Saccharomyces cerevisiae*. *Yeast* **32**, 711–720 (2015).
- 1112 125. Gibson, D. G. *et al.* Enzymatic assembly of DNA molecules up to several hundred kilobases.
1113 *Nat. Methods* **6**, 343–345 (2009).
- 1114 126. Gietz, R. D. Yeast transformation by the LiAc/SS carrier DNA/PEG method. *Methods Mol. Biol.*
1115 **1205**, 1–12 (2014).
- 1116 127. Boeke, J. D., LaCrute, F. & Fink, G. R. A positive selection for mutants lacking orotidine-5'-
1117 phosphate decarboxylase activity in yeast: 5-fluoro-orotic acid resistance. *Mol. Gen. Genet.*
1118 **197**, 345–346 (1984).
- 1119 128. Perez-Riverol, Y. *et al.* The PRIDE database and related tools and resources in 2019:
1120 improving support for quantification data. *Nucleic Acids Res.* **47**, D442–D450 (2019).
- 1121 129. Virtanen, P. *et al.* SciPy 1.0: fundamental algorithms for scientific computing in Python. *Nat.*
1122 *Methods* **17**, 261–272 (2020).
- 1123 130. The pandas development team. *pandas-dev/pandas: Pandas*. (2023).
1124 doi:10.5281/zenodo.8364959.
- 1125 131. Waskom, M. seaborn: statistical data visualization. *J. Open Source Softw.* **6**, 3021 (2021).
- 1126 132. Pedregosa, F. *et al.* Scikit-learn: Machine Learning in Python. *J. Mach. Learn. Res.* **12**, 2825–
1127 2830 (2011).
- 1128 133. Wickham, H. *et al.* Welcome to the tidyverse. *J. Open Source Softw.* **4**, 1686 (2019).